

Finite grid instability and spectral fidelity of the electrostatic Particle-In-Cell algorithm

C.-K. Huang^{a,*}, Y. Zeng^a, Y. Wang^a, M.D. Meyers^{a,b}, S. Yi^a, B. J. Albright^a

^a*Los Alamos National Laboratory, Los Alamos, NM, USA 87545*

^b*University of California, Los Angeles, CA, USA 90095*

Abstract

The origin of the Finite Grid Instability (FGI) is studied by resolving the dynamics in the 1D electrostatic Particle-In-Cell (PIC) model in the spectral domain at the single particle level and at the collective motion level. The spectral fidelity of the PIC model is contrasted with the underlying physical system or the gridless model. The systematic spectral phase and amplitude errors from the charge deposition and field interpolation are quantified for common particle shapes used in the PIC models. It is shown through such analysis and in simulations that the lack of spectral fidelity relative to the physical system due to the existence of aliased spatial modes is the major cause of the FGI in the PIC model.

Keywords: Finite Grid Instability, Particle-In-Cell, spectral fidelity, numerical instability

*Corresponding author

Email address: huangck@lanl.gov (C.-K. Huang)

1. Introduction

N-body type problems arise in many disciplines and underpins our understanding of complex dynamical systems like plasmas and the cosmos. In a typical N-body problem, the interaction in particle pairs can be of electrostatic, or electromagnetic, or gravitational in nature and each particle responds to a force that is the linear superposition of all one-to-one interactions it receives. Direct calculation of all one-to-one interactions of N_p particles has a computation cost of $O(N_p^2)$, therefore it is amenable to numerical simulation only when N_p is small. The PIC method [1], or more generally the particle-mesh method, is an efficient numerical method that reduces the computation complexity by introducing a computation grid and taking advantage of the linearity in the sum of one-to-one interactions. In the PIC method, the interaction among the particles is mediated by the grid through the Green's function of the interaction represented on the grid. The computation complexity is reduced from $O(N_p^2)$ to $O(N_g) + O(N_p)$, where N_g is the number of grid points. When the number of particles per cell $N_p/N_g \gg 1$, the gain in speedup is large ($\sim N_p$), therefore the PIC method is a popular choice in the *ab-initio* numerical simulation of N-body systems. However, two major problems arise in the PIC method due to the discrete grid: (1) the use of an Eulerian grid for the moments of the particle distribution and fields, in conjunction with individual Lagrangian particles in continuous phase space, implies an inherent inconsistency; (2) the grid representation of the Green's function is usually an approximation of the real Green's function in the continuous space.

Despite the computation efficiency of the PIC method and its wide-spread use, especially in plasma physics, common PIC models are vulnerable to an electrostatic numerical instability known as the Finite Grid Instability (FGI) [2, 3] (there is also an electromagnetic instability known as the numerical Cherenkov instability [4, 5, 6]). Early practitioners using the electrostatic PIC model to simulate plasma dynamics observed a heating effect to the plasma which depends on the numerical parameters, i.e., the grid size Δx and the number of particles per cell N_C . This numerical heating has been extensively studied since the early development of the PIC model and the empirical scaling of the heating time τ_H of FGI in a thermal plasma, which has the form $\omega_p \tau_H \sim (\lambda_D / \Delta x)^2 (N_D + N_C)$, is summarized in [1]. Here N_D is the number of particles in a Debye length λ_D , ω_p is the plasma frequency. It is also known that FGI comes from the aliased modes in the system due to the incompatibility between the Fourier spectra of the discrete Eulerian and continuous Lagrangian variables. (Numerical Cherenkov instability may also come from an Eulerian-Lagrangian mismatch in the convective derivative [4]). The numerical instabilities have been conventionally analyzed as unphysical resonances between physical and aliased modes [1, 4, 5, 6, 7, 8]. The locations and growth rates of the unstable modes have been solved for using linear dispersion analysis in limited, yet essential cases, i.e., for spatially uniform cold or Maxwellian distributions. It is worth noting that, unlike the two-stream type instabilities, for some commonly used electrostatic and electromagnetic PIC models, FGI can arise without the intersection of the physical and aliased modes [9, 8]. Analysis for more realistic and nonlinear simulations has not been carried out.

Various methods and numerical schemes to mitigate FGI have been proposed, including introducing grid interlacing [10] and random jiggling [10, 11], employing higher order particle shapes [9] and temporal/spatial filtering [12], implicit time differencing and enforcing the energy conservation property of the numerical algorithm between time steps [13, 14, 15, 16]. All these techniques have shown great promise with regard to the reduction of the instability growth rate. However, this is often achieved with substantial distortion/damping of the meaningful dynamics at the short wavelength scale or by sacrificing conservation properties (such as the loss of momentum conservation

in an energy conserving algorithm, which has long been debated in the development of the PIC models [1]). Recent rigorous work on energy conserving algorithm has led to a large improvement of the momentum conservation through nonlinear iterations [14].

The above efforts notwithstanding, the important questions about how and where FGI arises exactly remain to be answered. Previous works treat aliased modes as inherent in the system and study their properties and corresponding mitigation method. However, the origin of the numerical instabilities is clearly unphysical. Therefore, in principle a simulation plasma should be contrasted with the underlying continuous system, which has the same number of particles and particle shape as the simulation plasma, to determine the origin of the numerical instabilities. We call latter the physical system in the following, as it obeys a Vlasov equation for the shaped particles, as long as the same particle shape is used in defining the charge density from the particle and the electric field on the particle.

There are many choices about what to be contrasted between the PIC and the physical systems. Conservation properties and dispersion relationship have been used. It should be noted that one direct consequence of FGI in a PIC model without built-in energy (momentum) conservation property is, as can be expected, the gross violation of the energy (momentum) conservation. For this reason, recent efforts have been devoted to improve the energy and/or momentum conservation of the numerical scheme in order to control FGI. But it should be emphasized that conservation laws are desirable when eliminating the FGI, but they are neither necessary nor sufficient conditions. An isolated plasma system can exhibit various kinds of physical instabilities while strictly conserving momentum and energy. Furthermore, as total energy is a global property of the underlying microscopic processes and only one constraint on the degrees of freedom (two if total momentum is also considered) in the phase space, to understand what gives rise to FGI and its consequences, we need a better resolution into the dynamics. Linear dispersion, in which the eigen modes with complex Fourier frequency can be viewed as a way to resolve the (linearized) dynamics, is a better choice. However, such analysis is limited to special cases of the particle distribution and small perturbation amplitude. Insight from such analysis for the improvement to the numerical scheme is useful but not easy to obtain and applied to more general situations. Recently, symplectic PIC codes [17, 18] have also been developed, for which the symplectic structures of the Hamiltonian system is preserved. The symplectic structure may be a good choice to contrast the PIC and the physical systems, however, it is not clear how it is related to the numerical instabilities at present.

In this paper, we will study the FGI in the 1D electrostatic PIC models by spectrally resolving the dynamics at the single particle level, thus allowing us to identify the components in the model that lead to unphysical instability. The dynamics in PIC result from the superposition of the pairwise interactions as in a physical system. The major components of an electrostatic PIC model — the charge deposition, the field interpolation and the particle pusher, all operate on a single particle, while the field solver can be viewed as operating on the spatial Fourier modes. Therefore the use of the particle and spectral resolutions are natural choices for this purpose. Such a representation of the PIC models is given in section 2 and the spectral errors in PIC models are analyzed in section 3. As an alternative to the individual particle representation, one can also choose the modes of the collective particle motion as a representation. This has the advantage that the plasma dynamics can then be viewed as the collective wave-particle interactions and such couplings in a physical system and in a PIC model can also be contrasted. We note that the deposition, field interpolation and field solver only involve spatial operations at a fixed time, while the particle update in the pusher is a temporal operation in continuous space whose stability and convergence can be verified to rule

out its role in FGI. To facilitate simulation comparison with the physical system, the gridless model [19, 20, 21] is used, in which all components and elementary operations of the physical system are projected onto the finite Fourier basis. It is demonstrated in section 4 that the lack of spectral fidelity in the deposition, field interpolation is the major cause of the FGI. Finally we summarize in section 5.

2. Spectral representation of the PIC model

2.1. Charge deposition

Let's first look at the charge deposition scheme in Fourier space to understand the effect of aliasing. We will see that the most important effect in Fourier space is the summation over all Brillouin zones which is the result of a convolution process between a continuous spectrum and a periodic spectrum over Brillouin zones. The sampling needed to go from continuous space to a discrete grid is the cause of the latter spectrum.

In a grid-based model like PIC, the contribution of a particle at position \mathbf{x}_p ¹ and of total charge Q on the density grid \mathbf{r}_ρ is $\rho(\mathbf{r}_\rho) = QW(\mathbf{r}_\rho, \mathbf{x}_p)$, where \mathbf{r}_ρ is a vector on a uniform grid with grid size $\Delta\mathbf{x} = (\Delta x, \Delta y, \Delta z)$. The interpolation function for the deposition is $W(\mathbf{r}_\rho, \mathbf{r}) = W(|\mathbf{r}_\rho - \mathbf{r}|)$. Note that we have assumed the cell volume $V = \Delta x \Delta y \Delta z = 1$ and dropped it for clarity. The difference between a particle shape function $S(\mathbf{r})$ and a interpolation function $W(\mathbf{r}_\rho, \mathbf{r})$ is discussed in Appendix A. In the rest of this section, we will not distinguish these two and will use $S(\mathbf{r})$ for clarity, $\rho(\mathbf{r}_\rho) = QS_\rho(\mathbf{r}_\rho - \mathbf{x}_p)$. We define a transform (note this is not necessarily the proper Discrete Fourier Transform as \mathbf{r}_ρ may be shifted from the origin of the coordinate system, as will be shown later),

$$\tilde{\rho}(\mathbf{k}) = \sum_{\mathbf{r}_\rho} \rho(\mathbf{r}_\rho) e^{-i\mathbf{k}\cdot\mathbf{r}_\rho} = Q \sum_{\mathbf{r}_\rho} S_\rho(\mathbf{r}_\rho - \mathbf{x}_p) e^{-i\mathbf{k}\cdot\mathbf{r}_\rho}, \quad (2.1)$$

which can be viewed as the continuous Fourier transform of $\rho(\mathbf{r}) \sum_{\mathbf{r}_\rho} \delta(\mathbf{r} - \mathbf{r}_\rho)$, where $\rho(\mathbf{r}) = QS_\rho(\mathbf{r} - \mathbf{x}_p)$. Then the non-unitary inverse transform is

$$\rho(\mathbf{r}_\rho) = \frac{1}{8\pi^3} \int_{-\infty}^{\infty} \tilde{\rho}(\mathbf{k}) e^{i\mathbf{k}\cdot\mathbf{r}_\rho} d\mathbf{k}.$$

As $S_\rho(\mathbf{r})$ is a function in continuous space,

$$S_\rho(\mathbf{r}) = \frac{1}{8\pi^3} \int_{-\infty}^{\infty} \tilde{S}_\rho(\mathbf{k}') e^{i\mathbf{k}'\cdot\mathbf{r}} d\mathbf{k}'. \quad (2.2)$$

Then,

$$\tilde{\rho}(\mathbf{k}) = \frac{Q}{8\pi^3} \sum_{\mathbf{r}_\rho} \left(\int_{-\infty}^{\infty} \tilde{S}_\rho(\mathbf{k}') e^{i\mathbf{k}'\cdot(\mathbf{r}_\rho - \mathbf{x}_p)} d\mathbf{k}' \right) e^{-i\mathbf{k}\cdot\mathbf{r}_\rho} = \frac{Q}{8\pi^3} \int_{-\infty}^{\infty} \tilde{S}_\rho(\mathbf{k}') e^{-i\mathbf{k}'\cdot\mathbf{x}_p} \cdot \sum_{\mathbf{r}_\rho} e^{i(\mathbf{k}' - \mathbf{k})\cdot\mathbf{r}_\rho} \cdot d\mathbf{k}'. \quad (2.3)$$

Carrying out the infinite sum (see Appendix B), we obtain,

¹Italic bold font is used for vectors.

$$\tilde{\rho}(\mathbf{k}) = Q \sum_{\mathbf{q}} \psi(\mathbf{q} \cdot \mathbf{k}_g, \Delta \mathbf{r}_\rho) \tilde{S}_\rho(\mathbf{k}_g) e^{-i \mathbf{k}_g \cdot \mathbf{x}_p}, \quad (2.4)$$

and

$$\tilde{\rho}(\mathbf{k} + \mathbf{q}' \cdot \mathbf{k}_g) = \psi(-\mathbf{q}' \cdot \mathbf{k}_g, \Delta \mathbf{r}_\rho) \tilde{\rho}(\mathbf{k}),$$

where

$$\psi(\mathbf{q} \cdot \mathbf{k}_g, \Delta \mathbf{r}_\rho) = e^{i(\mathbf{q} \cdot \mathbf{k}_g) \cdot \Delta \mathbf{r}_\rho} \quad (2.5)$$

is a phase factor. $\mathbf{r}_\rho = \mathbf{r}_f + \Delta \mathbf{r}_\rho$ and \mathbf{r}_f is a reference grid that contains the origin of coordinate system. $\mathbf{k}_g = \mathbf{k} + \mathbf{q} \cdot \mathbf{k}_g$ is an vector alias of \mathbf{k} in the \mathbf{q} -th Brillouin zone $[\mathbf{q} \cdot \mathbf{k}_g - \mathbf{k}_g/2, \mathbf{q} \cdot \mathbf{k}_g + \mathbf{k}_g/2]$, $\mathbf{k}_g = (2\pi/\Delta x, 2\pi/\Delta y, 2\pi/\Delta z)$ and

$$\mathbf{q} = \begin{pmatrix} n & & \\ & m & \\ & & l \end{pmatrix}.$$

In the case that $\Delta \mathbf{r}_\rho \neq 0$, the spectra in Brillouin zones are not necessarily the same as a result of the transform defined in Eq. (2.1).

For a physical system consisting of particles of shape $S_\rho(\mathbf{r})$, a particle at position \mathbf{x}_p will contribute to the density as,

$$\tilde{\rho}(\mathbf{k}) = Q \tilde{S}_\rho(\mathbf{k}) e^{-i \mathbf{k} \cdot \mathbf{x}_p}, \quad (2.6)$$

where $\mathbf{k} \in (-\infty, \infty)$. For a gridless model which does charge deposition in Fourier space using truncated Fourier basis, Eq. (2.6) is used for a truncated domain $\mathbf{k} \in [-\mathbf{k}_c, \mathbf{k}_c]$, where \mathbf{k}_c is the cut-off wavenumber. To compare with a grid-based model, it is fair to set $\mathbf{k}_c = \mathbf{k}_g/2$ so both models have the same spectral resolution.

In Eq. (2.4) for the grid-based model and Eq. (2.6) for the physical or the gridless model, one can clearly see that the charge density is from the contribution $e^{-i \mathbf{k} \cdot \mathbf{x}_p}$ of a point-charge particle modified by its shape $\tilde{S}(\mathbf{k})$. Furthermore, the grid-based model has the aliasing effect in Fourier space which is absent in the physical or the gridless model, i.e., the summation over all Brillouin zones. The Brillouin zones exist due to the discreteness of the grid. The summation is due to the need to convolve the particle shape's continuous spectrum with a spectrum that includes Brillouin zones.

The ratio between $\tilde{\rho}(\mathbf{k})$ for the grid-based model, Eq. (2.4), and gridless models, Eq. (2.6), is,

$$\begin{aligned} (\tilde{S}_\rho(\mathbf{k}))^{-1} e^{i \mathbf{k} \cdot \mathbf{x}_p} \sum_{\mathbf{q}} \psi(\mathbf{q} \cdot \mathbf{k}_g, \Delta \mathbf{r}_\rho) \tilde{S}_\rho(\mathbf{k}_g) e^{-i \mathbf{k}_g \cdot \mathbf{x}_p} &= (\tilde{S}_\rho(\mathbf{k}))^{-1} \sum_{\mathbf{q}} \tilde{S}_\rho(\mathbf{k}_g) e^{-i(\mathbf{q} \cdot \mathbf{k}_g) \cdot (\mathbf{x}_p - \Delta \mathbf{r}_\rho)} \\ &\equiv G(\mathbf{x}_p - \Delta \mathbf{r}_\rho, \mathbf{k}; \tilde{S}_\rho(\mathbf{k})). \end{aligned} \quad (2.7)$$

$G(\mathbf{x}, \mathbf{k}; \tilde{S}_\rho(\mathbf{k}))$ determines the spectral error in the deposition for a particular particle shape $\tilde{S}_\rho(\mathbf{k})$ and will be quantified in section 3.

Eqs. (2.4) and (2.6) give the density for a single particle. For an infinite number of particles from a distribution $f(\mathbf{x}_p, \mathbf{v})$, we have,

$$\tilde{\rho}(\mathbf{k}) = \int d\mathbf{v} d\mathbf{x}_p f(\mathbf{x}_p, \mathbf{v}) Q \sum_{\mathbf{q}} \psi(\mathbf{q} \cdot \mathbf{k}_g, \Delta \mathbf{r}_\rho) \tilde{S}_\rho(\mathbf{k}_q) e^{-i \mathbf{k}_q \cdot \mathbf{x}_p} = \int d\mathbf{v} Q \sum_{\mathbf{q}} \psi(\mathbf{q} \cdot \mathbf{k}_g, \Delta \mathbf{r}_\rho) \tilde{S}_\rho(\mathbf{k}_q) \tilde{f}(\mathbf{k}_q, \mathbf{v}) \quad (2.8)$$

for the PIC model and,

$$\tilde{\rho}(\mathbf{k}) = \int d\mathbf{v} Q \tilde{S}_\rho(\mathbf{k}) \tilde{f}(\mathbf{k}, \mathbf{v}) \quad (2.9)$$

for the physical or gridless model. Apparently Eq. (2.8) and (2.9) differ in both amplitude and phase, however, such differences depend on $\tilde{f}(\mathbf{k}, \mathbf{v})$ and are difficult to quantify.

2.2. Field solver

For a physical system, Poisson's equation and electric field in continuous space are

$$\forall \mathbf{r} : -\nabla^2 \phi(\mathbf{r}) = \rho(\mathbf{r}), \mathbf{E}(\mathbf{r}) = -\nabla \phi(\mathbf{r}).$$

In Fourier space, this is completely equivalent to,

$$\forall \mathbf{k} : |[\mathbf{k}]|^2 \tilde{\phi}(\mathbf{k}) = \tilde{\rho}(\mathbf{k}), \tilde{\mathbf{E}}(\mathbf{k}) = -i[\mathbf{k}] \tilde{\phi}(\mathbf{k}), \quad (2.10)$$

where the operator $[\mathbf{k}] = \mathbf{k}$.

In a simulation, there are many ways to solve for the field. The common choices are,

- Use a spectral solver,

$$\forall \mathbf{k} \in [-\mathbf{k}_g/2, \mathbf{k}_g/2] : |[\mathbf{k}]_{sp}|^2 \tilde{\phi}(\mathbf{k}) = \tilde{\rho}(\mathbf{k}), \tilde{\mathbf{E}}(\mathbf{k}) = -i[\mathbf{k}]_{sp} \tilde{\phi}(\mathbf{k}) \quad (2.11)$$

where $[\mathbf{k}]_{sp} = \mathbf{k}$. In this case, \mathbf{E} and ρ are collocated on the same grid which is chosen to be the reference grid, i.e., $\mathbf{r}_E = \mathbf{r}_\rho = \mathbf{r}_f$, $\tilde{\mathbf{E}}(\mathbf{k}) = \sum_{\mathbf{r}_f} \mathbf{E}(\mathbf{r}_f) e^{-i \mathbf{k} \cdot \mathbf{r}_f}$ and $\tilde{\rho}(\mathbf{k}) = \sum_{\mathbf{r}_f} \rho(\mathbf{r}_f) e^{-i \mathbf{k} \cdot \mathbf{r}_f}$. We also have $\tilde{\mathbf{E}}(\mathbf{k} + \mathbf{k}_g) = \tilde{\mathbf{E}}(\mathbf{k})$ and $\tilde{\rho}(\mathbf{k} + \mathbf{k}_g) = \tilde{\rho}(\mathbf{k})$.

- Use finite difference on Poisson's equation and the potential for which the spectral representation is,

$$\forall \mathbf{k} : |[\mathbf{k}]_{fd}|^2 \tilde{\phi}(\mathbf{k}) = \tilde{\rho}(\mathbf{k}), \tilde{\mathbf{E}}(\mathbf{k}) = -i[\mathbf{k}]_{fd} \tilde{\phi}(\mathbf{k}). \quad (2.12)$$

Here, $[\mathbf{k}]_{fd} = ([k_x]_{fd}, [k_y]_{fd}, [k_z]_{fd})$, $[k_\alpha]_{fd}$ for $\alpha \in \{x, y, z\}$ is related to the Fourier representation of the finite difference operator. $\tilde{\rho}(\mathbf{k}) = \sum_{\mathbf{r}_\rho} \rho(\mathbf{r}_\rho) e^{-i \mathbf{k} \cdot \mathbf{r}_\rho}$ and $\tilde{E}_\alpha(\mathbf{k}) = \sum_{\mathbf{r}_{E_\alpha}} E_\alpha(\mathbf{r}_{E_\alpha}) e^{-i \mathbf{k} \cdot \mathbf{r}_{E_\alpha}}$

from the transform defined in Eq. (2.1), which in turn gives the usual form of $[k_\alpha]_{fd}$, e.g., $[k_x]_{fd} = k_x \text{sinc}(k_x \Delta x / 2)$. As central differencing is typically used, $[k_x]_{fd}$, $[k_y]_{fd}$, $[k_z]_{fd}$ are purely real functions. Since E_α and ρ may be defined on different grids from the reference grid, so in general $\tilde{E}_\alpha(\mathbf{k} + \mathbf{k}_g) = \psi(-\mathbf{k}_g, \Delta \mathbf{r}_{E_\alpha}) \tilde{E}_\alpha(\mathbf{k})$, $\tilde{\rho}(\mathbf{k} + \mathbf{k}_g) = \psi(-\mathbf{k}_g, \Delta \mathbf{r}_\rho) \tilde{\rho}(\mathbf{k})$ and $\Delta \mathbf{r}_{E_\alpha} = \mathbf{r}_{E_\alpha} - \mathbf{r}_f$, $\Delta \mathbf{r}_\rho = \mathbf{r}_\rho - \mathbf{r}_f$.

Another possible choice is to use spectral solver on Poisson's equation and finite difference on the potential, as done in the code XES1 [1]. It is clear that none of these choices for the field solver has systematic phase error, however, using finite difference inevitably introduces systematic amplitude error.

2.3. Field interpolation

In PIC, after the field on the grid $\mathbf{E}(\mathbf{r}_E)$ is calculated, it is interpolated to the j -th particle's position according to

$$\mathcal{E}(\mathbf{x}_j) = \sum_{\mathbf{r}_E} S_E(\mathbf{x}_j - \mathbf{r}_E) \mathbf{E}(\mathbf{r}_E), \quad (2.13)$$

where the particle shape function is $S_E(\mathbf{r}) = \int_{-\infty}^{\infty} d\mathbf{k} \tilde{S}_E(\mathbf{k}) e^{i\mathbf{k}\cdot\mathbf{r}} / 8\pi^3$ and may be different than $S_\rho(\mathbf{r})$ in charge deposition. Then,

$$\mathcal{E}(\mathbf{x}_j) = \frac{1}{8\pi^3} \int_{-\infty}^{\infty} d\mathbf{k} \tilde{S}_E(\mathbf{k}) e^{i\mathbf{k}\cdot\mathbf{x}_j} \sum_{\mathbf{r}_E} \mathbf{E}(\mathbf{r}_E) e^{-i\mathbf{k}\cdot\mathbf{r}_E} = \frac{1}{8\pi^3} \int_{-\infty}^{\infty} d\mathbf{k} \tilde{S}_E(\mathbf{k}) e^{i\mathbf{k}\cdot\mathbf{x}_j} \tilde{\mathbf{E}}(\mathbf{k}). \quad (2.14)$$

This means that $\mathcal{E}(\mathbf{k}) = \tilde{S}_E(\mathbf{k}) \tilde{\mathbf{E}}(\mathbf{k})$, i.e., no aliasing effect for a particular mode $\tilde{\mathbf{E}}(\mathbf{k})$. This is consistent with the idea that only sampling leads to aliasing, interpolation does not. Note that this view is for single mode analysis, for the total force on a particle, we need to integrate over all \mathbf{k} , so the summation over all Brillouin zones reappears. Generally, we have $\tilde{E}_\alpha(\mathbf{k} + \mathbf{k}_g) = \psi(-\mathbf{k}_g, \Delta \mathbf{r}_{E_\alpha}) \tilde{E}_\alpha(\mathbf{k})$ for each component $\alpha = x, y, z$, so

$$\mathcal{E}_\alpha(\mathbf{x}_j) = \frac{1}{8\pi^3} \int_{-\mathbf{k}_g/2}^{\mathbf{k}_g/2} d\mathbf{k} \tilde{E}_\alpha(\mathbf{k}) \sum_{\mathbf{q}} \psi(-\mathbf{q} \cdot \mathbf{k}_g, \Delta \mathbf{r}_{E_\alpha}) \tilde{S}_E(\mathbf{k}_q) e^{i\mathbf{k}_q \cdot \mathbf{x}_j}. \quad (2.15)$$

In a physical model, the field on the particle can be directly reconstructed from the Fourier components,

$$\mathcal{E}(\mathbf{x}_j) = \frac{1}{8\pi^3} \int_{-\infty}^{\infty} d\mathbf{k} \tilde{S}_E(\mathbf{k}) e^{i\mathbf{k}\cdot\mathbf{x}_j} \tilde{\mathbf{E}}(\mathbf{k}). \quad (2.16)$$

In a gridless model, only modes from the truncated Fourier basis, i.e., $\mathbf{k} \in [-\mathbf{k}_g/2, \mathbf{k}_g/2]$, are used,

$$\mathcal{E}(\mathbf{x}_j) = \frac{1}{8\pi^3} \int_{-\mathbf{k}_g/2}^{\mathbf{k}_g/2} d\mathbf{k} \tilde{S}_E(\mathbf{k}) e^{i\mathbf{k}\cdot\mathbf{x}_j} \tilde{\mathbf{E}}(\mathbf{k}). \quad (2.17)$$

Similar to the charge deposition, the integrands in the above equations for the PIC, physical (or gridless) model differ by a ratio,

$$\begin{aligned} (\tilde{S}_E(\mathbf{k}))^{-1} e^{-i\mathbf{k}\cdot\mathbf{x}_j} \sum_{\mathbf{q}} \psi(-\mathbf{q} \cdot \mathbf{k}_g, \Delta \mathbf{r}_{E_\alpha}) \tilde{S}_E(\mathbf{k}_q) e^{i\mathbf{k}_q \cdot \mathbf{x}_j} &= (\tilde{S}_E(\mathbf{k}))^{-1} \sum_{\mathbf{q}} \tilde{S}_E(\mathbf{k}_q) e^{i(\mathbf{q} \cdot \mathbf{k}_g) \cdot (\mathbf{x}_j - \Delta \mathbf{r}_{E_\alpha})} \\ &= G(\Delta \mathbf{r}_{E_\alpha} - \mathbf{x}_j, \mathbf{k}; \tilde{S}_E(\mathbf{k})). \end{aligned} \quad (2.18)$$

3. Spatial phase and amplitude errors in PIC

Depending on the initial conditions, driving force, equilibrium etc., the plasma that we are trying to model may exhibit a host of unstable modes itself. So to distinguish the physical and numerical instabilities, one needs to look for the differences between the two systems. As the spatial components of the PIC loop, i.e., charge deposition, field solver and field interpolation, are now

spectrally resolved, it is informative to investigate the errors in the spectral domain involved in these components. In fact, it turns out that all these three components have errors in the spectral domain. Such errors can be systematic or random in nature (e.g. from round-off error) and we will only focus on the former.

It is particularly worthwhile to understand the role that the systematic spectral errors play in the numerical instabilities. The phase error plays a crucial role in the development of instabilities, and in many cases determines whether the system is stable or not. On the other hand, the amplitude error typically affects the instability growth rate. In some other cases, e.g., for instabilities with amplitude threshold or some parametric instabilities, the mode amplitude can also determine the stability. However, most numerical instabilities we encounter and need to mitigate in the PIC model are not known to be of this type.

3.1. Spectral error for shaped particle

Next, we will quantify the phase and amplitude errors of the PIC model compared to the gridless model, which is a computationally feasible but costly model for approximating the physical system with both spectral fidelity (up to the cut-off wave-number) and conservative properties.

For the field solver, it is easy to see from Eqs. (2.11), (2.12) that neither the finite difference or spectral solver introduces systematic phase error. There is systematic amplitude error in the finite difference solver but none in the spectral solver.

In general, Eq. (2.8) indicates that the deposited charge density has systematic amplitude and phase errors which depend on the particle distribution function. But for a system with finite number of shaped particles, we can further discern these errors by resolving the contributions from individual particles using Eq. (2.7). As summing each individual particle's contribution to the charge density is a linear process, we do not expect such summation to generate additional errors other than round-off. In addition, field interpolation is naturally written for one particle in Eq. (2.15). Therefore, for a single particle, Eqs. (2.7) and (2.18) give the errors that can be quantified for a specific particle shape. For an orthogonal coordinate system and corresponding deposition and force interpolation, $G(\mathbf{x}, \mathbf{k}; \tilde{S}(\mathbf{k})) = \prod_{\alpha=x,y,z} g_\alpha(\alpha/\Delta\alpha, k_\alpha; \tilde{s}_\alpha(k_\alpha))$ for $\tilde{S}(\mathbf{k}) = \prod_{\alpha=x,y,z} \tilde{s}_\alpha(k_\alpha)$. For Cartesian coordinate, we only need to determine the spectral errors for one particular dimension, e.g., $g(x/\Delta x, k; \tilde{s}(k)) = \tilde{s}(k)^{-1} \sum_q \tilde{s}(k_q) e^{-iqk_g x}$ for x direction.

Since $g(x/\Delta x, k; \tilde{s}(k))$ is periodic in x ,

$$g(x + 1, k; \tilde{s}(k)) = g(x, k; \tilde{s}(k)),$$

and symmetric in k for symmetric shape function $\tilde{s}(-k) = \tilde{s}(k)$,

$$g(x, -k; \tilde{s}(-k)) = g(x, k; \tilde{s}(k)),$$

one only needs to determine $g(x, k; \tilde{s}(k))$ for $x \in [0, 1]$ and $k \in [0, k_g/2]$. For the most commonly used B-spline particle shapes $\tilde{s}_\mu(k)$ of order μ and the Gaussian function $\tilde{s}_G(k)$, the systematic spectral errors $g(x, k; \tilde{s}(k))$ can be analytically quantified.

For B-spline particle shapes, $\tilde{s}_\mu(k) = [\text{sinc}(k\Delta x/2)]^{\mu+1}$, the infinite sum in $g(x, k; \tilde{s}_\mu)$ can be evaluated into a compact form using the Hurwitz-Lerch transcendent $\Phi(z, s, a) = \sum_{n=0}^{\infty} z^n (n+a)^{-s}$ to give,

$$g(x, k, \tilde{s}_\mu) = \left(\frac{-k\Delta x}{2\pi} \right)^{\mu+1} \left[e^{-i2\pi x} \Phi \left((-1)^{\mu+1} e^{-i2\pi x}, \mu+1, 1 + \frac{k\Delta x}{2\pi} \right) \right. \\ \left. + \Phi \left((-1)^{\mu+1} e^{i2\pi x}, \mu+1, \frac{-k\Delta x}{2\pi} \right) \right]. \quad (3.1)$$

Similarly, for a Gaussian function of width $\sigma\Delta x$, $s_G(x; \sigma) = e^{-x^2/(\sigma\Delta x)^2}/(\sqrt{\pi}\sigma\Delta x)$, $\tilde{s}_G(k; \sigma) = e^{-(k\sigma\Delta x/2)^2}/\sqrt{2\pi}$, the infinite sum in $g(x, k; \tilde{s}_G)$ can be evaluated using the elliptic theta function $\vartheta_3(u, q) = 1 + 2 \sum_{n=1}^{\infty} q^{n^2} \cos(2nu)$ to give,

$$g(x, k, \tilde{s}_G) = \frac{1}{\sqrt{\pi}\sigma} e^{\sigma^2(k\Delta x/2+ix/\sigma^2)^2} \vartheta_3 \left(k\Delta x/2 + ix/\sigma^2, e^{-1/\sigma^2} \right). \quad (3.2)$$

Although $s_G(x; \sigma)$ is a valid particle shape but not a valid interpolation function, one can define a new function $\tilde{s}(k) = \tilde{s}_G(k; \sigma)\tilde{s}_\mu(k)$ such that the corresponding $s(x)$ is a valid interpolation function. For example, for $\mu = 0$, we have $\tilde{s}_{Erf}(k; \sigma) \equiv \tilde{s}_G(k; \sigma)\tilde{s}_0(k) = e^{-(k\sigma\Delta x/2)^2} \text{sinc}(k\Delta x/2)/\sqrt{2\pi}$ and $s_{Erf}(x; \sigma) = [\text{Erf}(\frac{1}{2\sigma} - \frac{x}{4\sigma\Delta x}) + \text{Erf}(\frac{1}{2\sigma} + \frac{x}{4\sigma\Delta x})]/(2\Delta x)$, where $\text{Erf}(x)$ is the error function. It is not clear whether $g(x, k; \tilde{s}_{Erf})$ has a compact analytic form but numerical evaluation in Fig. 2 shows $g(x, k; \tilde{s}_{Erf})$ is similar to $g(x, k; \tilde{s}_G)$.

The amplitude and phase of $g(x, k, \tilde{s}_\mu)$, $g(x, k, \tilde{s}_G)$ and $g(x, k, \tilde{s}_{Erf})$ are shown in Figs. 1 and 2. The general trends in Figs. 1 and 2 are that (1) larger amplitude and phase errors occur at higher k ; and (2) the wider the particle shape, the errors are more concentrated at high k . Both amplitude and phase errors depend on the particle's position in the cell, except for the amplitude error for s_0 (nearest grid point). For the phase error, the largest error occurs when the particle is in the middle of the cell.

Comparing $g(x, k, \tilde{s}_\mu)$ in Fig. 1, another salient observation is that the phase error improves slowly with the increase of the order of the particle shape. Also the dependence of the errors on the particle position does not seem to go away quickly as the order is increased, despite stronger attenuation to the high k modes. As will be shown at the end of section 3.2, the spectral errors, especially their dependences on the particle position, play a key role in determining the growth rate of most unstable mode in the linear FGI case, while the attenuation to the high k modes due to $\tilde{S}(\mathbf{k})$ and $\tilde{S}'(\mathbf{k})$ in the front factors in Eq. (2.7) and (2.18) enlarges the stability domain, but at the expense of accuracy of the high k modes. The high order B-spline particle shapes offer both benefits but the latter benefit can also be achieved via a low-pass filter that is independent of the particle position.

3.2. Relation between the linear instability and the spectral error

The value of $\tilde{s}(k)$ in and outside the fundamental Brillouin zone $-k_g/2 < k < k_g/2$ play different roles in the linear grid instability. The latter value is related to the spectral errors $g(x, k; \tilde{s}(k))$. In order to distinguish their roles, it is instructive to inspect the linear dispersion equation Eq. (C.7) in the limit $\Delta t \rightarrow 0$ for a 1D cold drifting plasma with velocity v_0 ,

$$1 - \frac{1}{k^2} \sum_q \frac{\tilde{s}^2(k_q) k_q^2}{(\omega - k_q v_0)^2} = 0, \quad (3.3)$$

where we also assume $\tilde{s}_\rho = \tilde{s}_E = \tilde{s}$, $[k]^2 = k^2$ and $\kappa(k_q) = k_q$ for simplicity.

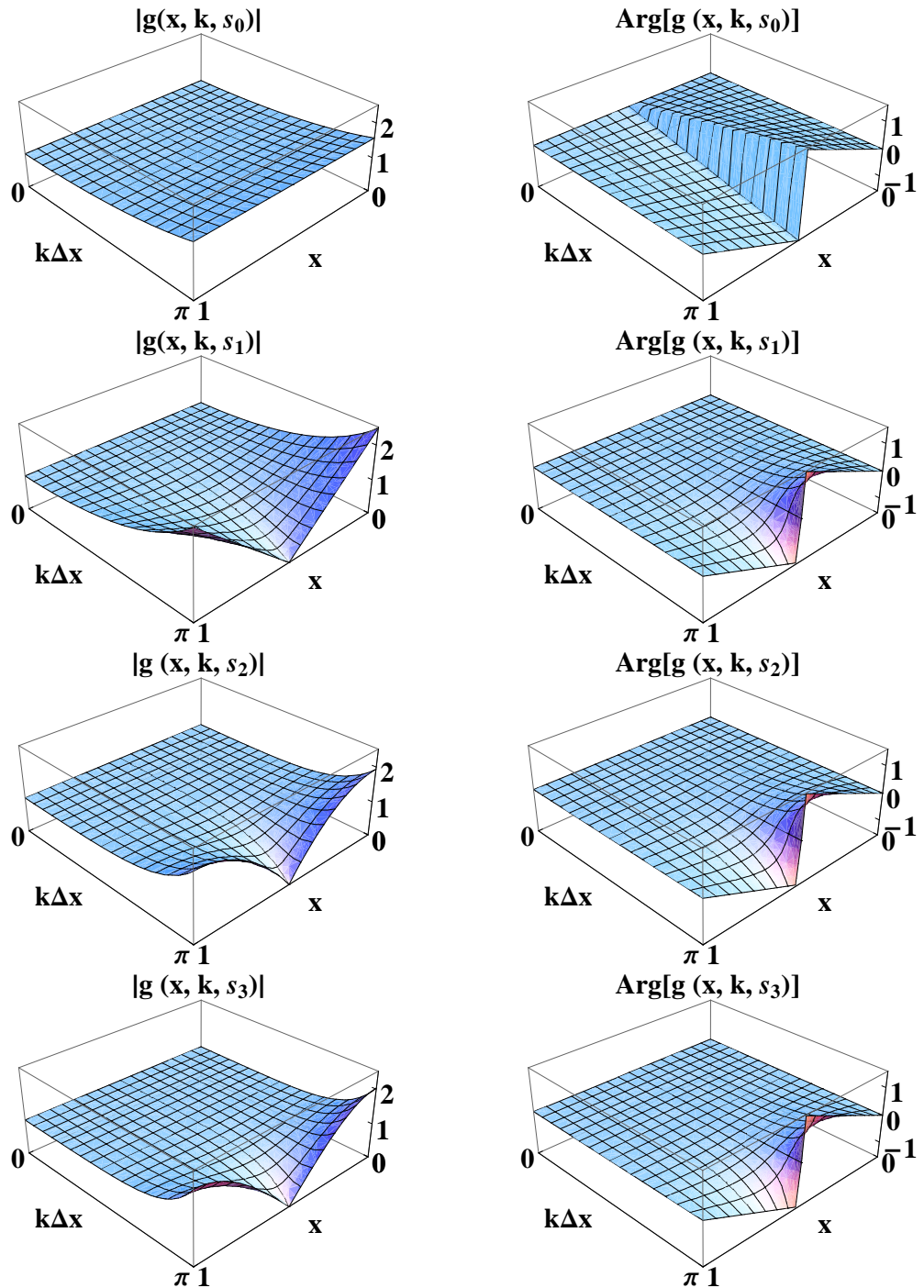


Figure 1: The amplitude (left column) and phase (right column) of $g(x, k, \tilde{s}_\mu)$ for $\mu = 0, 1, 2, 3$, which correspond to nearest grid point, linear, quadratic, cubic particle shapes, respectively.

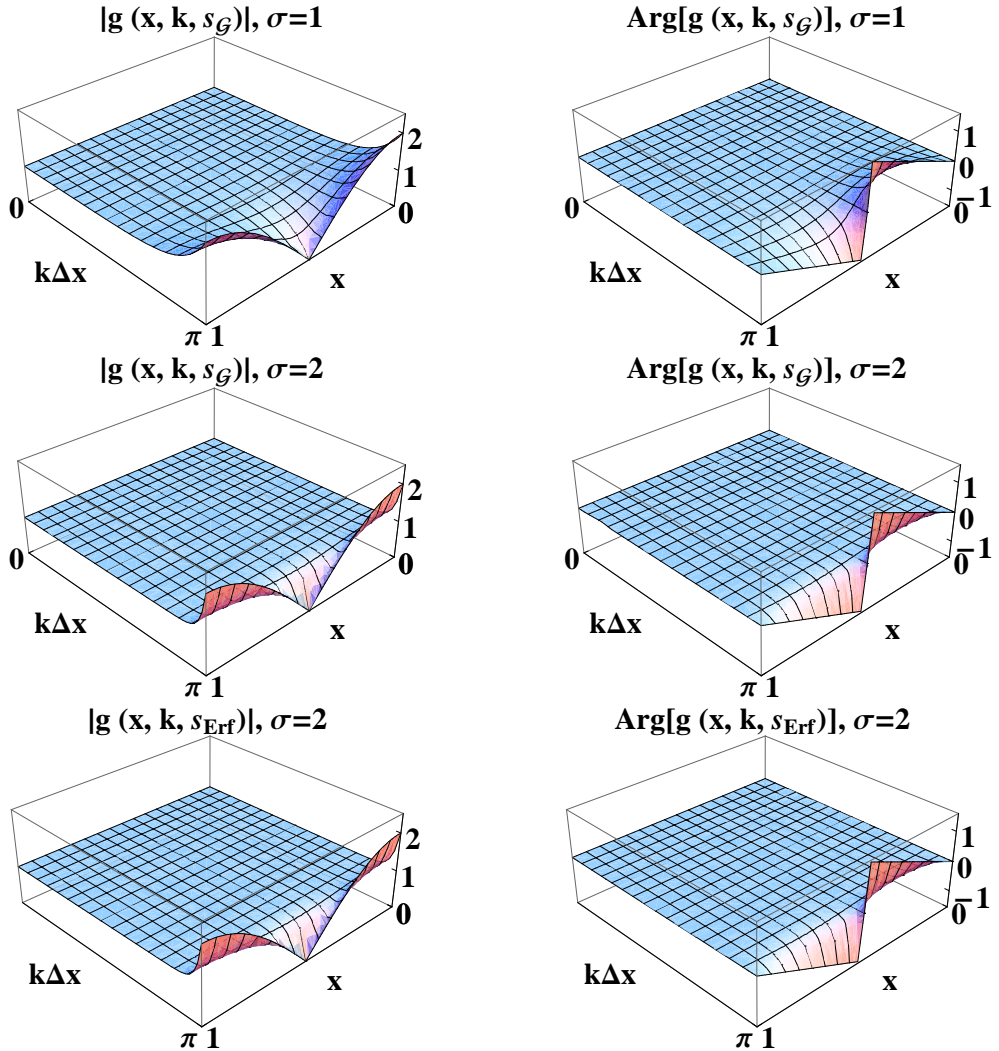


Figure 2: The amplitude (left column) and phase (right column) of $g(x, k; \tilde{s}_G)$ for the Gaussian shape $s_G(x; \Delta x)$ (top row), $s_G(x; 2\Delta x)$ (middle row) and of $g(x, k; \tilde{s}_{Erf})$ for the $s_{Erf}(x; 2\Delta x)$ shape (bottom row), respectively.

As $\sum_q \tilde{s}(k_q) e^{-iqk_g x} = \tilde{s}(k) g(x/\Delta x, k; \tilde{s}(k))$, inverse Fourier transform with respect to x gives $\tilde{s}(k_q) = g_q \tilde{s}(k)$, where $g_\alpha \equiv \tilde{g}(\alpha, k; \tilde{s}(k)) = \Delta x \int dx e^{-i2\pi\alpha x} g(x, k; \tilde{s}(k))$ is discrete at $\alpha = q$ due to the periodicity of $g(x, k; \tilde{s}(k))$ in x . For n th order B-spline shape, $g_q = (-k/k_q)^{n+1}$; for $\tilde{s}_{Erf}(k; \sigma)$ shape, $g_q = -k/k_q \cdot e^{\sigma^2[(k\Delta x/2)^2 - (k\Delta x/2 + q\pi)^2]}$. Keeping only the 0th and q th terms, Eq. (3.3) can be rewritten as,

$$1 - \tilde{s}^2(k) \left[\frac{1}{\Omega^2} + \frac{g_q^2 k_q^2 / k^2}{(\Omega - k_g v_0)^2} \right] = 0, \quad (3.4)$$

where $\Omega = \omega - k_g v_0$ and $-k_g/2 < k < k_g/2$.

In Eq. (3.4), $\tilde{s}(k)$ and g_q affect the instability domain and growth rate differently. For the model dispersion in Eq. (3.4), mode stability requires $\tilde{s}(k) \lesssim k_g v_0$ (see Appendix C). So for sufficiently small $\tilde{s}(k)$ in the fundamental Brillouin zone, there is no instability for a particular k . However, this is achieved at the expense of the dispersion accuracy of the physical modes, since $\tilde{s}(k)$ can be seen as a renormalization of Ω . While $g_q = \tilde{s}(k_q)/\tilde{s}(k)$, which is closely related to the spectral errors $g(x, k; \tilde{s}(k))$, affects the alias modes thus the instability only. More specifically, g_q has a large effect on the instability growth rate but little on the stability domain. g_q is real and can be written as a sum of the Fourier coefficients of the amplitude and phase components of $g(x, k; \tilde{s}(k))$,

$$g_q = \sum_l A_l \Theta_{q-l} \quad (3.5)$$

where $A_l = \Delta x \int dx e^{-i2\pi l x} |g(x, k; \tilde{s}(k))|$ and $\Theta_{q-l} = \Delta x \int dx e^{-i2\pi(q-l)x + i\text{Arg}[g(x, k; \tilde{s}(k))]}$. The dominating terms in Eq. (3.5) is $A_0 \Theta_q$ and $A_q \Theta_0$ as both A_l and Θ_l are highly peaked at $l = 0$. Therefore the q th alias mode appears mainly because the presence of the amplitude or phase errors that is position-dependent and modulated at the q th harmonics of the grid. For the common B-spline particle shapes, $A_0 \Theta_q$ dominates at high k , therefore the amplitude error is more important, while at lower k , $A_q \Theta_0$ dominates, i.e., the phase error is more important.

The most unstable mode k^{max} in the dispersion Eq. (3.4) can be obtained from $\tilde{s}(k^{max}) \approx k_g v_0$. Its normalized growth rate is

$$\omega_i^{max} \approx \frac{3^{1/2}}{2 \cdot 2^{1/3}} \tilde{s}(k^{max})^{1/3} (k_q^{max}/k^{max})^{2/3} g_q^{2/3} \approx \frac{3^{1/2}}{2 \cdot 2^{1/3}} (k_g v_0)^{1/3} (1 + qk_g/k^{max})^{2/3} g_q^{2/3}. \quad (3.6)$$

Therefore, smaller $\tilde{s}(k)$ in the fundamental Brillouin zone (but keeping g_q the same) actually leads to smaller k^{max} and higher maximum growth rate, while smaller $|g_q|$ (but keeping $\tilde{s}(k)$ in the fundamental Brillouin zone the same) lowers the maximum growth rate. This indicates that a particle shape with a high contrast between the fundamental and higher order Brillouin zones, i.e., small $|g_q|$ that translates to small position dependent spectral errors, is beneficial when aliasing is unavoidable.

3.3. Spectral fidelity of the collective modes

Now it is clear that the systematic spectral errors in the deposition and field interpolation occur at the individual particle level, but the overall errors from an ensemble of plasma particles are less transparent. To this end, we can analyze how these errors manifest themselves in the collective motion of a finite number of particles. To simplify this analysis, an initially cold beam of N_p particles moving at velocity V_0 is assumed, but the analysis is not restricted to this velocity

distribution. Each particle has charge Q , mass m . The system is periodic with length L and N_g cells, $\Delta x = L/N_g$ is the cell size. When there is no perturbation, the j -th particle is located at X_j and particles are equally spaced with distance $\Delta X = L/N_p$. The particle's position x_j is perturbed at $t = 0$ and then evolves self-consistently. The displacement of the particle is $\delta x(X_j, t) = x_j(t) - X_j$ and can be expanded into Fourier modes

$$\delta x(X_j, t) = N_p^{-1} \sum_{\frac{\pi}{\Delta X} \geq |K|} \tilde{\delta x}(K, t) e^{i K X_j} = 2N_p^{-1} \sum_{\frac{\pi}{\Delta X} \geq K \geq 0} A(K, t) \cos(K X_j + \theta(K, t)),$$

where $\tilde{\delta x}(K, t) = A(K, t) e^{i \theta(K, t)} = \sum_j \delta x(X_j, t) e^{-i K X_j}$, $A(K, t)$ and $\theta(K, t)$ are the mode amplitude and phase of the collective motion of these N_p particles. The drift motion of the beam is described by the $K = 0$ mode.

Assuming these particles have shape $\tilde{s}(k)$, their contribution to the density of mode k in the periodic physical system (or a gridless model) is

$$\tilde{\rho}(k) = Q \sum_j \tilde{s}(k) e^{-ikx_j(t)} = Q \tilde{s}(k) \sum_j e^{-ik \left[X_j + 2N_p^{-1} \sum_{\frac{\pi}{\Delta X} \geq K \geq 0} A(K, t) \cos(K X_j + \theta(K, t)) \right]}, \quad (3.7)$$

where $|k| < \pi/\Delta x$. the phase factor in this sum can be written, using the Jacobi-Anger expansion, as

$$\begin{aligned} & e^{-ik \left[X_j + 2N_p^{-1} \sum_{\frac{\pi}{\Delta X} \geq K \geq 0} A(K, t) \cos(K X_j + \theta(K, t)) \right]} \\ &= e^{-ikX_j} \cdot \prod_{\frac{\pi}{\Delta X} \geq K \geq 0} \left\{ \sum_{\nu_K} i^{\nu_K} J_{\nu_K}(-2kA(K, t)/N_p) \cdot e^{i\nu_K[KX_j + \theta(K, t)]} \right\} \\ &= e^{-ikX_j} \cdot \sum_{\nu_0, \dots, \nu_K} \left\{ e^{i \sum (\nu_K K) \cdot X_j + i \sum \nu_K \cdot [\theta(K, t) + \pi/2]} \cdot \prod_{\nu_0, \dots, \nu_K} J_{\nu_K}(-2kA(K, t)/N_p) \right\}. \end{aligned} \quad (3.8)$$

where ν_K is an integer for each mode K in $\frac{\pi}{\Delta X} \geq K \geq 0$, $J_{\nu_K}(x)$ is the ν_K -th Bessel function of the first kind. $\sum_{\nu_0, \dots, \nu_K} (\prod_{\nu_0, \dots, \nu_K})$ is a sum (product) over all combination of ν_K s and $\sum \nu_K$ is a sum of every ν_K for $\frac{\pi}{\Delta X} \geq K \geq 0$.

Summing Eq. (3.8) over X_j and using $\sum_{\nu_0=-\infty}^{\infty} J_{\nu_0}(x) = 1$ gives,

$$\tilde{\rho}(k) = N_p Q \tilde{s}(k) \sum_{\nu_1, \dots, \nu_K} \left\{ \delta \left(k - m k_P - \sum (\nu_K K) \right) \cdot e^{i \sum \nu_K \cdot [\theta(K, t) + \pi/2]} \cdot \prod_{\nu_1, \dots, \nu_K} J_{\nu_K}(-2kA(K, t)/N_p) \right\}, \quad (3.9)$$

where $k_P = 2\pi/\Delta X = N_p 2\pi/L$ and m is an integer.

Eq. (3.9) describes the contribution from the Fourier modes of the collective motion to the Fourier modes of the density, where the first, second and third terms in the curly bracket determining the mode coupling relation, phase and strength, respectively. The $\pi/2$ in the phase factor comes

from the phase difference between particle's displacement and the density. Note that Eq. (3.9) is valid for arbitrary number of particles and arbitrary spectrum/amplitude of the collective modes. Due to the finite number of particles in a system, the mk_P term in the argument of the delta function introduces a physical coupling due to the "particle aliasing" effect of the collective mode. Typically we are interested in the case $k \ll k_P$, thus this effect couples a low k mode and a very high K collective mode efficiently only when ν_K is a small number. Furthermore, the coupling coefficient $J_{\nu_K} (-2kA(K, t)/N_p)$ would be small when there are sufficient large number of particles, $N_p \gg 1$, so practically we may take $m = 0$ and ignore this effect in a physical system for most situations.

Next we investigate the coupling among collective modes and density modes only. This can be illustrated by understanding how a single collective mode couples to the density perturbation first. For a collective mode spectrum with a single mode K_0 , $A(K_0) \neq 0$, while $A(K \neq K_0) = 0$. Since $J_{\nu_K}(0) \neq 0$ only when $\nu_K = 0$, so we have $\delta(k - \sum(\nu_K K)) = \delta(k - \nu_{K_0} K_0)$. This corresponds to the excitation of the fundamental mode $k = K_0$ and its harmonics $k = \nu_{K_0} K_0$ with the mode coupling coefficient being $s(\nu_{K_0} K_0) e^{i\nu_{K_0} [\theta(K_0, t) + \pi/2]} \cdot J_{\nu_{K_0}} (-2\nu_{K_0} K_0 A(K_0, t)/N_p)$. Similarly, when there are two collective modes K_0 and K_1 , their beating will result in density perturbation at mode $k = \nu_{K_0} K_0 + \nu_{K_1} K_1$ with the coupling coefficient being $s(\nu_{K_0} K_0 + \nu_{K_1} K_1) e^{i[\nu_{K_0} \theta(K_0, t) + \nu_{K_1} \theta(K_1, t) + \pi/2 \cdot (\nu_{K_0} + \nu_{K_1})]} \cdot J_{\nu_{K_0}} (-2kA(K_0, t)/N_p) J_{\nu_{K_1}} (-2kA(K_1, t)/N_p)$. From this, the coupling for the density perturbation involving more collective modes can be generalized.

The density perturbation created by the collective modes in turn drives more collective modes of the particles through the electric field. We define the electric field on the particle as a function of X_j ,

$$\mathcal{E}(X_j, t) = E(x_j(t)) = N_g^{-1} \sum_k \tilde{s}(k) \tilde{E}(k) e^{ikx_j(t)} = N_g^{-1} \sum_k \frac{-i}{[k]} \tilde{s}(k) \tilde{\rho}(k) e^{ikx_j(t)},$$

whose Fourier transform with regard to X_j is,

$$\mathcal{E}(K, t) = N_g^{-1} \sum_j \sum_k \frac{-i}{[k]} \tilde{s}(k) \tilde{\rho}(k) e^{i[kx_j(t) - KX_j]}.$$

Here, $[k]$ is the effective operator from the field solver. Similar to the phase factor for the density in Eq. (3.8), the phase factor in the above equation can be expanded and the sum over X_j can be carried out to give,

$$\begin{aligned} \mathcal{E}(K, t) &= \frac{N_p}{N_g} \sum_k \frac{-i}{[k]} \tilde{s}(k) \tilde{\rho}(k) \sum_{\nu_1, \dots, \nu_{K'}} \left\{ \delta \left(K - k - mk_P - \sum (\nu_{K'} K') \right) e^{i \sum \nu_{K'} [\theta(K', t) + \pi/2]} \right. \\ &\quad \left. \cdot \prod_{\nu_1, \dots, \nu_{K'}} J_{\nu_{K'}} (2kA(K', t)/N_p) \right\}. \end{aligned} \quad (3.10)$$

The relation between $\mathcal{E}(K, t)$ and $\tilde{\rho}(k)$ (or $E(k)$) depends on the argument of the delta function and the sum over k , therefore it is more complicated than that between $\tilde{\rho}(k)$ and $\tilde{x}(K, t)$ in Eq. (3.9). Again we may ignore the particle aliasing effect in the collective mode when $N \gg 1$. Then for the simplest case of a collective motion with a single mode K_0 , a non-zero value of $\prod_{\nu_1, \dots, \nu_{K'}} J_{\nu_{K'}} (2kA(K', t)/N_p)$ requires that $\nu_{K' \neq K_0} = 0$, therefore, $\sum \nu_{K'} = \nu_{K_0}$, $\sum (\nu_{K'} K') =$

$\nu_{K_0} K_0$. Coupling to $\mathcal{E}(K, t)$ thus comes from $\tilde{\rho}(k = K - \nu_{K_0} K_0)$, which is not necessarily the harmonics of K_0 . When the collective motion involves two modes K_0 and K_1 , coupling to $\mathcal{E}(K, t)$ can come from $\tilde{\rho}(k = K - \nu_{K_0} K_0 - \nu_{K_1} K_1)$ for any ν_{K_0} and ν_{K_1} .

Finally, the evolution of the collective modes is determined by the equation of motion

$$d(\delta x(K, t))/dt^2 = \frac{Q}{m} \mathcal{E}(K, t), \quad (3.11)$$

which is an ordinary differential equation (ODE). Clearly, regardless of whether it is written in a continuous or discrete time variable, this step does not introduce spectral errors in K -space.

Now, Eqs. (3.9), (3.10) and (3.11) are the coupled equations describing the evolution of the collective modes in the physical system of a cold beam. When the discrete time version of Eq. (3.11) is used, these equations represent a discrete-time analog of the physical system. If Eq. (3.11) is discretized using a scheme consistent with the underlying ODE, i.e., the solution of the discretized equation approaches that of the ODE when the discretization step $\Delta t \rightarrow 0$, then a numerical instability, if occurring in this discrete-time system, will exhibit dependence on Δt . Therefore, a convergence test can discern a numerical instability due to discretization in time. Early study of FGI already established that the numerical heating rate is independent of the time step, therefore time discretization cannot be the reason of FGI. From the single particle analysis of the systematic spectral errors presented earlier in this section, we can see that another possibility of the numerical instability in PIC is the spectral errors in the deposition and field interpolation due to the aliasing effect. In fact, for the PIC model, Eqs. (3.9) and (3.10) take on the following forms,

$$\begin{aligned} \tilde{\rho}(k) = N_p Q \sum_q \tilde{s}(k_q) \sum_{\nu_1, \dots, \nu_K} & \left\{ \delta \left(k_q - m k_P - \sum (\nu_K K) \right) e^{i \sum \nu_K [\theta(K, t) + \pi/2]} \right. \\ & \left. \cdot \prod_{\nu_1, \dots, \nu_K} J_{\nu_K} (-2k_q A(K, t)/N_p) \right\}, \end{aligned} \quad (3.12)$$

$$\begin{aligned} \mathcal{E}(K, t) = & \frac{N_p}{N_g} \sum_q \sum_{|k| \leq k_g/2} \frac{-i}{[k_q]} \tilde{\rho}(k_q) \cdot \tilde{s}(k_q) \cdot \sum_{\nu_1, \dots, \nu_{K'}} & \left\{ \delta \left(K - k_q - m k_P - \sum (\nu_{K'} K') \right) \right. \\ & \left. \cdot e^{i \sum \nu_{K'} [\theta(K', t) + \pi/2]} \prod_{\nu_1, \dots, \nu_{K'}} J_{\nu_{K'}} (2k_q A(K', t)/N_p) \right\}, \end{aligned} \quad (3.13)$$

where k has been replaced by its alias k_q and a sum of all aliases is taken.

Compared with Eqs. (3.9) and (3.10), Eqs. (3.12) and (3.13) lack the spectral fidelity to the physical system, i.e., they contain not only phase and amplitude errors, but also unphysical mode couplings. As will be shown in the next section, such lack of spectral fidelity is the major cause of the finite grid instability.

4. Comparison of the gridless model and the PIC models

In this section, we compare the 1D non-relativistic electrostatic simulation results of a numerical plasma that is susceptible to the finite grid instability, for various PIC models and from the gridless

model. The simplest simulation is that of a single-mode electrostatic oscillation in a cold plasma with a drift. While this mode will generate high harmonics, such system should be stable for a long time. During this period, the plasma should remain cold, i.e., the local momentum spread is zero. The three spatial components of the numerical scheme — the charge deposition, the field solver and the field interpolation, are implemented in the PIC/finite-difference mode and/or the gridless mode. The mode history from the simulations are compared, the focus here is not the accuracy of the simulation but to understand the roles of the amplitude and phase errors in the finite grid instability.

The simulation box has dimensionless size $L = 2\pi c/\omega_p$ and $N = 33$ cells. The initial plasma density n_0 is constant across the box. $N_C = 300$ particles per cell is used for the electrons and the ions constitute a uniform neutralizing background. The electrons are equally spaced and a sinusoidal displacement $\delta x(x_{p0}) = AL \cos(2\pi Mx_{p0}/L)/(2\pi M)$ is applied to initialize a density perturbation, where M is the mode number and x_{p0} is the unperturbed particle position. The density perturbation is given by $n_1(x)/n_0 = -\partial \delta x / \partial x = A \sin(2\pi Mx/L)$ for point particles and the actual amplitude will be smaller by $s(k = 2\pi M/L)$ when a shaped particle is used in the simulation. The electron initial velocity is the sum of the drift velocity $V_0 = 0.01c$ and perturbed velocity $\delta V = AL\omega_p \sin(2\pi Mx/L)/(2\pi M)$, where c is the speed of light.

Results are compared in Fig. 3 for four simulations with $\omega_p \Delta t = 0.2$: (1) the momentum conserving PIC model [1] with linear particle shape; (2) the momentum conserving PIC model with quadratic particle shape; (3) the energy conserving PIC model [13] with quadratic particle shape; and (4) the electrostatic gridless model [20, 21] with quadratic particle shape. For all PIC models compared, the initial small-amplitude single-mode perturbation ($A \sim 10^{-2}$ for mode $K = 9$) excites all the modes in the system at a level of $\sim 10^{-6}$ immediately after the first step. Then, it is observed that mode $k = 15$, which is an alias mode from the second harmonics $K = 18$ of the initial perturbation in the adjacent Brillouin zone, grows exponentially in all PIC models. The growth rate is higher for the lower order particle shape used in the momentum conserving PIC models. Although the initial amplitude of mode $k = 15$ is higher in the energy conserving PIC model with quadratic particle shape due to the lower order, i.e., linear, particle shape used in field interpolation, the growth rate is about the same as in the momentum conserving PIC with quadratic shape. Following the growth of mode $k = 15$, mode $k = 6$ also grows at a similar rate, which appears to be a result of the beating between modes $k = 9$ and $k = 15$. Other exponential growing modes before $\omega_p t < 50$, e.g., modes $k = 3$ and $k = 12$ may also result from beating. These modes grow to an amplitude comparable to the initial perturbation during $\omega_p t \sim 50 - 100$, after which a wide spectrum of modes are excited. As a result of the interaction with a wide spectrum of waves, the phase space plots in Fig. 4 show heated electron distributions in all PIC models, while the momentum (energy) is relatively constant in the momentum (energy) conserving model by design. Comparing with the gridless model for which the perturbation remains single-mode and the electrons stay cold during the simulation, it can be seen that the development of the wide-band spectrum and the heating of the electrons are clearly numerical effects. Such numerical artifacts result from the lack of spectral fidelity in the PIC model.

It should be noted that the gridless model improves not only the spectral accuracy of the dynamics, but also the energy and momentum conservation of the simulation model. In Fig. 4, the gross loss of energy (momentum) conservation in the momentum (energy) conserving PIC models are correlated with the saturation of the unstable mode growth. Furthermore, despite the 2nd order accurate leap-frog scheme used for the time advance in all models, only the gridless model

exhibits energy conservation (and possibly for momentum conservation) that scales like $O(\Delta t^3)$ in this numerical instability test. For the gridless model, the energy conservation is improved by about a factor of 1000 when the time step is decreased by a factor of 10 to $\omega_p \Delta t = 0.02$, while the momentum conservation is already at the machine precision for $\omega_p \Delta t = 0.2$ thus does not improve further. For the energy conserving model, the heating in phase space, mode history and growth rate are essentially unchanged when the time step is decreased to $\omega_p \Delta t = 0.02$, while the momentum conservation is only slightly improved and the energy conservation is improved by about a factor of 10. The heating and unstable mode growth behave similarly in the momentum conserving model, but neither the energy or momentum conservation improves as time step is decreased to $\omega_p \Delta t = 0.02$. The superior conservative properties of the gridless model may be due to the fact that it can be derived from the action principle using a truncated Fourier series [21] and the resulting finite dimension dynamical system possesses spectral fidelity to the physical system. The advantage of the variational models [21, 17, 18] and the spectral fidelity in conservation properties and numerical stability deserve further study but will not be pursued here.

To understand the relative importance of the spectral fidelity in the deposition/interpolation and the field solver, in particular the role of amplitude and phase errors, simulations are carried out using the momentum conserving PIC model with the deposition/interpolation and the field solver implemented in gridless mode respectively. The results are shown in Fig. 5. Operating the field solver in the gridless mode effectively turns the finite difference PIC model into a spectral PIC model, which improves upon the systematic amplitude error and random spectral errors in a finite difference solver. The benefit is seen in Fig. 5 where the dominate modes are those separated modes (mode 3, 6, 9, 12, 15) up to $\omega_p t = 200$, but the onset of whole spectrum excitation, similar to those shown in Fig. 3, is delayed to $\omega_p t \sim 400$ in a longer simulation (not shown). The growth rate of mode 15 is about the same as in the case with a finite difference solver and the electron phase space shows similar heating. Thus a spectral solver that improves amplitude and random errors does not qualitatively change the characteristics of the simulation. Upon adopting the gridless deposition and field interpolation (but keeping the finite difference field solver), which improves both the systematic phase and amplitude errors, the results are essentially similar to those of the gridless model, with a higher floor of the background modes. This confirms that the major loss of the spectral fidelity in PIC occurs in the deposition and the field interpolation where their phase errors play important roles in FGI.

The dynamics shown in Fig. 3 involves nonlinear coupling of a large range of modes as the system evolves, but at the early time the unstable dynamics grows predominately from the interaction between density mode $k = \pm 15$ and the collective mode $K = 18$ which is excited by the initial perturbation at $K = 9$. To quantitatively determine the behavior of such interaction, we can set $\delta x(K, t) = A e^{i\omega_r t} = A_0 e^{i(\omega t + \theta_0)}$, where $\omega = \omega_r - i\omega_i$, $\delta x(K, 0) = A_0 e^{i\theta_0}$ and $A = A_0 e^{\omega_i t}$. Inserting this into the coupled Eqs. (3.11), (3.12) and (3.13), and ignoring the particle aliasing effect then $N \gg 1$, one obtains,

$$\begin{aligned} -A_0 \omega^2 e^{i(\omega t + \theta_0)} &= \frac{N_p^2 Q^2}{N_g m} \sum_{q'} \sum_q \frac{-i}{[k_{q'}]} \tilde{s}(k_q) \cdot \tilde{s}(k_{q'}) \delta(k_q - \nu_K K) \delta(K - k_{q'} - \nu_{K'} K) \\ &\quad \cdot e^{i(\nu_K + \nu_{K'}) \cdot (\omega_r t + \theta_0 + \pi/2)} J_{\nu_K}(-2k_q A_0 e^{\omega_i t} / N_p) J_{\nu_{K'}}(2k_{q'} A_0 e^{\omega_i t} / N_p), \end{aligned} \quad (4.1)$$

This can be simplified by equating the time varying phase on both sides of Eq. (4.1) and setting the arguments of the delta functions to zero, i.e., using the following relationships for the mode

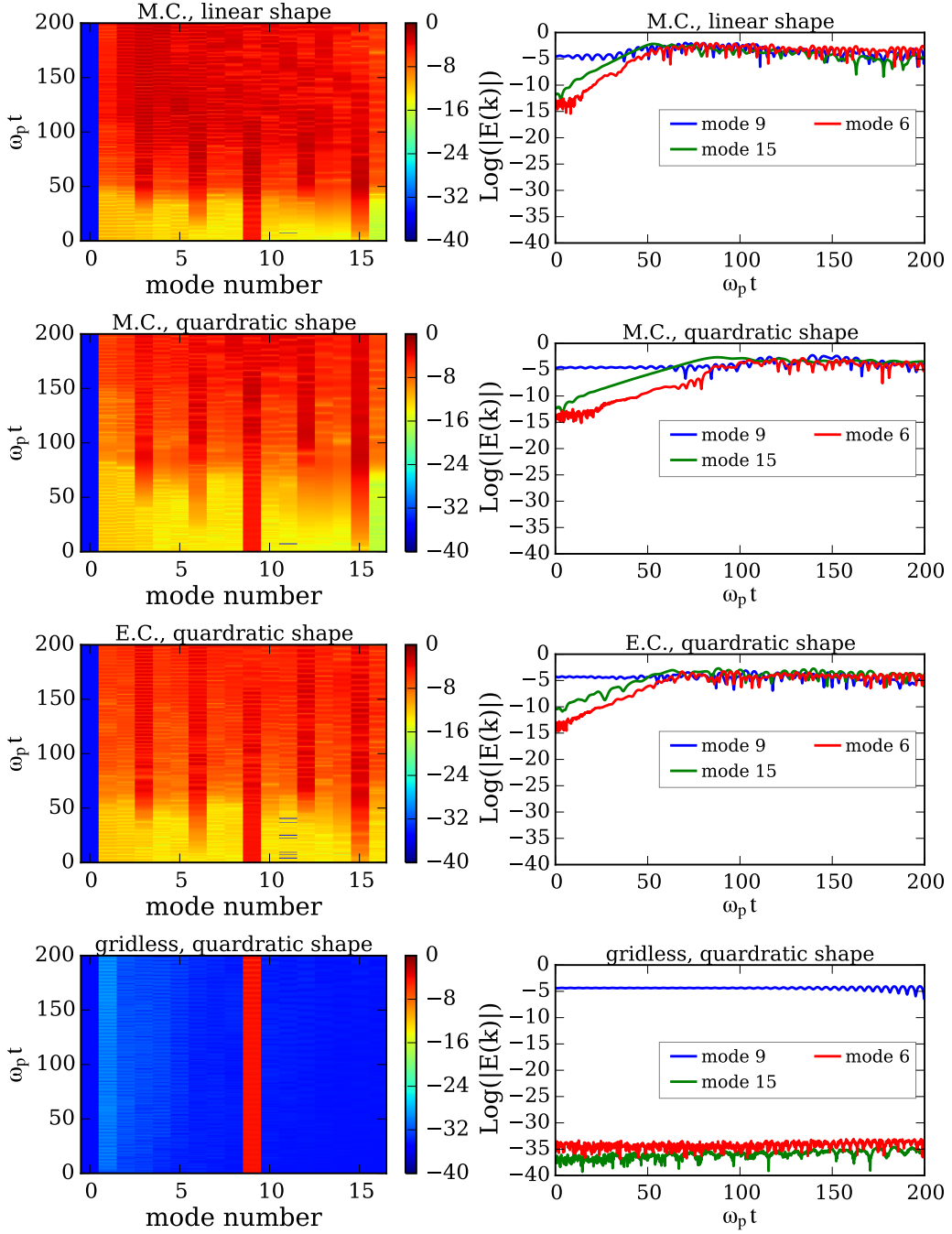


Figure 3: Simulation mode spectrum from various models. Left column: full mode spectrum $\ln(|E(k)|)$ as a function of time. Right column: evolution of the mode amplitude for the perturbation — mode $k = 9$, alias of its second harmonic — mode $k = 15 (= 33 - 9 \times 2)$ and the beat between them — mode $k = 6 (= 15 - 9)$. The four rows from top to bottom correspond to (1) the momentum conserving (M.C.) PIC model with linear particle shape; (2) the momentum conserving PIC model with quadratic particle shape; (3) the energy conserving (E.C.) PIC model with quadratic particle shape; and (4) the gridless model with quadratic particle shape.

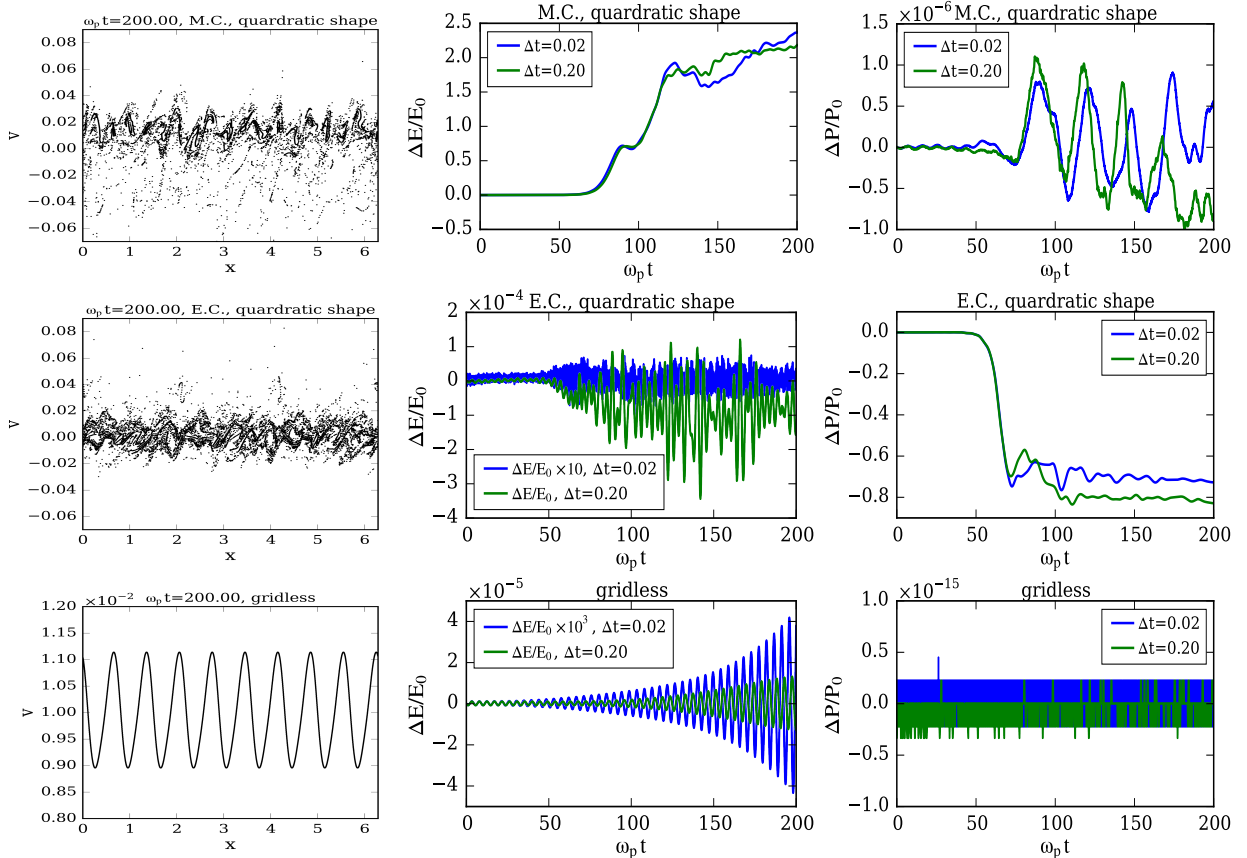


Figure 4: Electron phase space at the end of the simulation (left column), energy (middle column) and momentum (right column) conservation from various models. The energy and momentum conservation are shown for $\omega_p \Delta t = 0.2$ (green curves) and $\omega_p \Delta t = 0.02$ (blue curves). The three rows from top to bottom correspond to (1) the momentum conserving (M.C.) PIC model with quadratic particle shape; (2) the energy conserving (E.C.) PIC model with quadratic particle shape; and (3) the gridless model with quadratic particle shape.

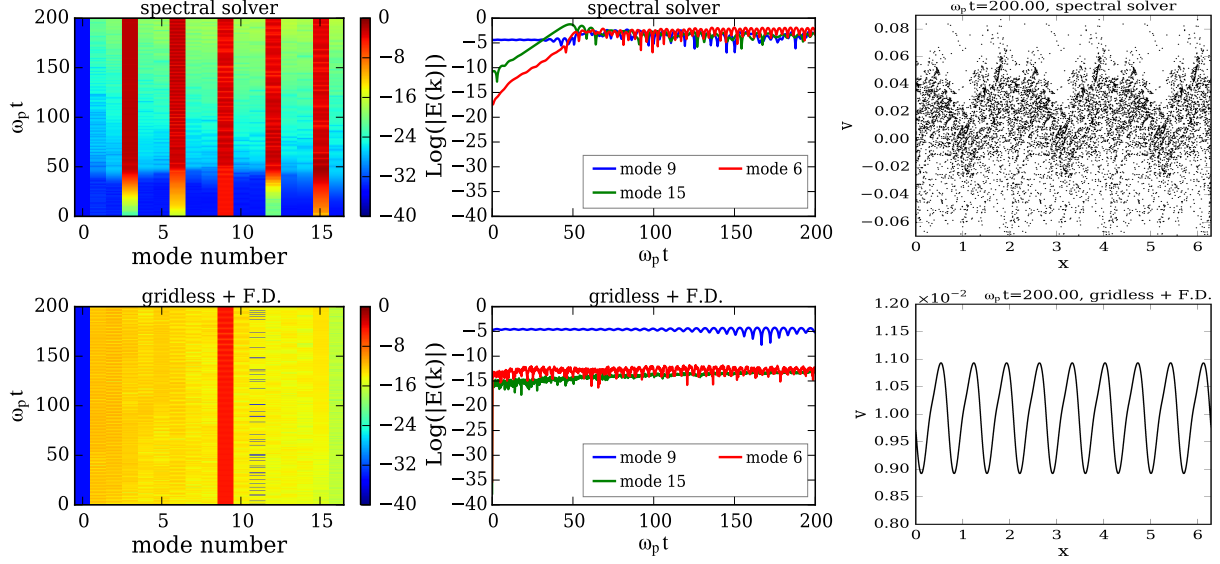


Figure 5: The mode spectrum (left column), amplitudes of mode 9, 15, 6 (middle column), and electron phase space from a PIC model (right column) with (1) a spectral solver (top row); (2) gridless deposition and field interpolation (bottom row).

coupling,

$$\begin{aligned} \nu_K + \nu_{K'} &= 1, \\ q &= q', \\ \nu_K &= k_q/K, \\ \nu_K, q &\in \mathbf{Z}, \end{aligned} \quad (4.2)$$

to give,

$$\omega^2 e^{\omega_i t} \Delta n_K^0 = -2K \sum_{\nu_K=k_q/K} \frac{\tilde{s}^2(\nu_K K)}{[\nu_K K]} J_{\nu_K}(-\nu_K e^{\omega_i t} \Delta n_K^0) J_{(1-\nu_K)}(\nu_K e^{\omega_i t} \Delta n_K^0). \quad (4.3)$$

where the normalization $n \rightarrow n/n_p$, $\omega \rightarrow \omega/\omega_p$, $t \rightarrow \omega_p t$, $Q \rightarrow N_g/N_p$, $Q/m \rightarrow 1$, is used and $\Delta n_K^0 = 2KA_0/N_p$ is the normalized initial density perturbation due to the collective mode K . The summation in Eq. (4.3) is over all integers ν_K and q that satisfy $\nu_K = k_q/K = (k + qk_g)/K$. For the above example, $k = \pm 15$, $K = 18$ and $k_g = 33$, we can rewrite the infinite summation to be,

$$\sum_{\nu_K=k_q/K} = \sum_{l \in \mathbf{Z}},$$

with $q = 6l \mp 1$, $\nu_K = 11l \mp 1$. For $|x| \lesssim 0.7$, $|J_{\nu_K}(-\nu_K x) J_{1-\nu_K}(\nu_K x)|$ drops quickly as $|\nu_K|$ increases, so in practice only the $l = 0$ term needs to be included in the above sum until the coupling is nonlinear.

Thus, Eq. (4.3) becomes,

$$\omega^2 e^{\omega_i t} \Delta n_K^0 \approx -2K \left[\frac{\tilde{s}^2(-K)}{[-K]} J_{-1}(e^{\omega_i t} \Delta n_K^0) J_2(-e^{\omega_i t} \Delta n_K^0) + \frac{\tilde{s}^2(K)}{[K]} J_1(-e^{\omega_i t} \Delta n_K^0) J_0(e^{\omega_i t} \Delta n_K^0) \right]. \quad (4.4)$$

The first (second) term on the right hand side results from the coupling through mode $k = 15$ ($k = -15$). The coupling from the second term is much stronger than that from the first term through mode when the perturbation amplitude is small, i.e., when $e^{\omega_i t} \Delta n_K^0 \ll 1$. In fact the second term leads to absolute instability ($\omega_r = 0$), while the first term leads to oscillatory solution ($\omega_i = 0$). Therefore, an initially small perturbation grows exponentially until saturation and then oscillates at that level. The linear growth rate can be obtained by dropping the first term and Taylor expanding the Bessel functions in the second term, which gives,

$$\omega_i \approx \tilde{s}(K) \sqrt{|K/[K]|}, \quad (4.5)$$

which does not depend on the drift velocity V_0 . When $e^{\omega_i t} \Delta n_K^0 \approx 1.84$, the RHS of (4.4) is zero, therefore the normalized instability saturation time is

$$t_{sat} \approx \ln(1.84/\Delta n_K^0)/\omega_i. \quad (4.6)$$

Note that the linear FGI in section 3.2 is different than the case discussed here. For the former case, unstable modes grow independently from particle noise. Each unstable mode involves the fundamental of the collective motion that can be resolved by the grid (harmonics have been dropped in the linear analysis), and the corresponding density perturbation which also contains alias modes that cause the instability. For the latter case, the collective motion cannot be resolved by the grid. Therefore the density mode contains alias modes only and the instability can be more severe than the former case, e.g., for the simulation with large amplitude perturbation. Also, unlike the former FGI case which is convective and has stability domains, the latter instability is absolute and has no stability domain as long as $K > k_g$ and $\tilde{s}(K) > 0$.

The linear growth rate from Eq. (4.5), $\omega_i \approx 0.21$, and the instability saturation time from Eq. (4.6), $t_{sat} \approx 46.5$, are compared to the simulation shown in Fig. 6, in which only collective mode $K = 18$ and electric field modes $k = \pm 15$ are kept and an initial perturbation in the mode $K = 18$ is applied. Solving Eq. (3.4) for modes $k = \pm 15$ gives $\omega_i \approx 0.04$ which is much smaller than the actual grow rate. This simulation result is also in close agreement with the example shown in Fig. 5, for the dynamics of mode $k = 15$ in the linear growth stage up to the saturation of the instability, indicating the early unstable dynamics is due to the coupling between $K = 18$ and $k = \pm 15$ modes. However, the detail dynamics after saturation in the latter simulation involves more mode coupling, thus requiring a more complete treatment similar to the above analysis.

5. Summary

In this paper, the origin of the FGI is studied by employing particle and spectral resolutions into the dynamics of the 1D electrostatic PIC model and by contrasting the spectral fidelity of the PIC model with respect to the underlying physical system (or the gridless model). The particle resolution can be either adopted for individual particle or for the collective motion. The use of the particle and spectral resolutions are not the only options for this purpose, but are suitable ones as the particle dynamics consist of pair-wise interactions and can also be viewed as collective wave-particle interactions.

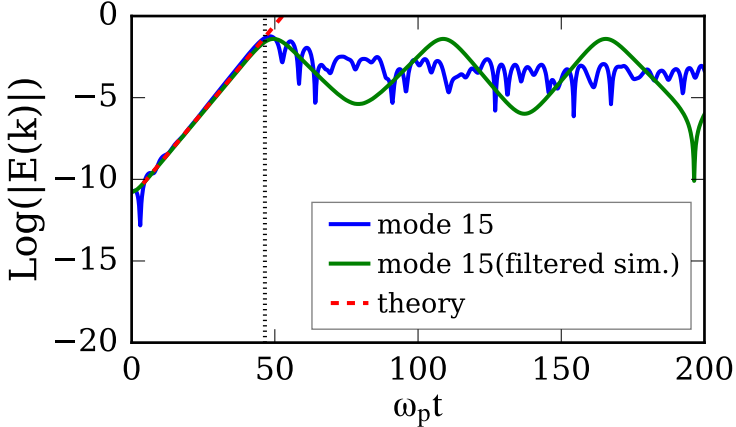


Figure 6: Comparison of the FGI growth (red, dashed, $\omega_i \approx 0.21$) and the saturation time (black, dotted, $t_{sat} \approx 46.5$) predicted by Eq (4.5) and Eq. (4.6), respectively, with $\ln|E(k=15)|$ in a PIC simulation using a 2nd order particle shape and a spectral field solver (green curve). Eq. (3.4) gives $\omega_i \approx 0.04$. The simulation is initialized with a perturbation in the collective mode $K = 18$ such that $\Delta n_K^0 = 10^{-4}$. Only the collective mode $K = 18$ and the electric field modes $k = \pm 15$ are kept in the simulation. Other numerical parameters are the same as in the simulation in Fig. 5 that employs a spectral solver, no mode filtering and an initial perturbation in mode $K = 9$ such that $\Delta n_K^0 = 10^{-2}$ (blue curve).

At the individual particle level, the charge deposition and field interpolation operations of the PIC models exhibit systematic spectral errors relative to the physical system (or gridless model) due to the existence of the spatial alias modes from the use of the discrete grid in conjunction with Lagrangian particles in continuous space. In principle, these errors can be calculated for arbitrary particle shape, and surprisingly, they have relatively compact analytic forms shown in Eq. (3.1) for the B-spline particle shapes and in Eq. (3.2) for the Gaussian particle shape. These forms allow us to understand the effects in the spectral domain from using shaped particles in the PIC models. It is observed that these systematic spectral errors depend on both $k\Delta x$ and the particle's normalized position in the cell. These errors are directly related to the instability growth rate but they improve slowly with the increase of the order (smoothness) of the B-spline particle shape. Another benefit of using higher order particle shape is the stronger damping to the short-wavelength modes in the fundamental Brillouin zone which can enlarge the stability domain. Such a damping effect also applies to the physical modes and may be achieved using a spatial mode filter on the grid which has a lower computation cost and does not depend on individual particle's position.

At the collective motion level, as it is shown in Eqs. (3.12) and (3.13), the charge deposition and field interpolation introduce unphysical mode couplings which eventually result in amplitude and phase errors in the collective modes. This is also due to the aliasing of the spatial modes. Within the framework of collective wave-particle interactions, Eqs. (3.9), (3.10) and (3.11) are the coupled equations describing the evolution of the collective modes in the physical system, while Eqs. (3.12) and (3.13) and the discrete time version of Eq. (3.11) are the counterparts for the PIC model, whose convergence with respect to time step can be verified to rule out the time discretization as a possible origin of the FGI. In fact, early works on FGI already indicated that the numerical heating rate is independent of the time step with the leap-frog advance, while our result also shows that the growth rates of the unstable modes are not affected by the time step, making it clear the cause of FGI can only be the lack of spectral fidelity of Eqs. (3.12) and (3.13) as compared to Eqs. (3.9) and

(3.10). In this regard, the difference between the PIC model and the physical system (or gridless model) is technical, not fundamental — with a properly-chosen particle shape such that $s(k) = 0$ for $|k| > k_g/2$, we recover Eqs. (3.9) and (3.10) from Eqs. (3.12) and (3.13) for $|k| \leq k_g/2$, thus making the PIC models effectively a gridless model. This opens the question of the optimal compact particle shapes for the PIC model. Finally, as with many physical instabilities which result from the constructive feedback of modes, it can be understood that the systematic spectral errors play important roles in the development of FGI. This finding is verified in the simulation comparison with the gridless model and may help the design of a PIC model with better stability.

6. Acknowledgements

We are grateful to many of our colleagues for their valuable comments to this work. One of the authors (C. H.) would like to thank Prof. D. F. Escande for his lectures in Los Alamos National Laboratory (LANL) which motivated the analysis using the collective modes. This work is supported by the U.S. Department of Energy through the LDRD program at LANL.

Appendix A. Particle shape function and interpolation function

The function $S(\mathbf{r})$ is used to define particle shape in phase space (for PIC, the shape in velocity dimension is assumed to be a Delta function) and the function $W(\mathbf{r}_g, \mathbf{r})$ is used in the charge deposition and field interpolation. The PIC method can be derived from the Vlasov equation using the distribution function of shaped particles [22], which reveals that any symmetric function, $S(\mathbf{r}) = S(-\mathbf{r})$, or $\tilde{S}(\mathbf{k}) = \tilde{S}(-\mathbf{k})$, can be used as long as the averaged fields on the particle is defined as in Eq. (6) of [22]. Self-force consideration and momentum conservation require that the same function be used for charge deposition and field interpolation. The other requirement on the shape function is $\int S(\mathbf{r}) d\mathbf{r} = 1$, or $\tilde{S}(\mathbf{k} = 0) = 1$, while for a valid interpolation function in PIC, charge conservation requires $\sum_{\mathbf{r}_g} W(\mathbf{r}_g, \mathbf{r}) = 1$. From the Poisson summation, this requires

$$\sum_{\mathbf{r}_g} W(\mathbf{r}_g, \mathbf{r}) = \sum_{\mathbf{q}} \tilde{W}(\mathbf{q} \cdot \mathbf{k}_g) e^{i(\mathbf{q} \cdot \mathbf{k}_g) \cdot \mathbf{r}} = 1,$$

which is equivalent to $\tilde{W}(\mathbf{k} = 0) = 1$ and $\tilde{W}(\mathbf{q} \cdot \mathbf{k}_g) = 0$ for $n^2 + m^2 + l^2 \neq 0$. Therefore a particle shape function is not necessarily an interpolation function, e.g., a linear particle shape function with a width of half the grid size is not a valid interpolation function. But valid interpolation functions are true particle shape functions, e.g., the family of B-spline interpolation functions used in PIC. Furthermore, the convolution of an arbitrary shape function $S(\mathbf{r})$ with these B-spline interpolation functions results in valid interpolation functions. In this paper, we will not distinguish the particle shape function and the interpolation function unless necessary and will use $S(\mathbf{r})$ for clarity.

Appendix B. Aliasing and phase factor

From the Poisson summation formula $\sum_{n=-\infty}^{\infty} e^{ik_0 n \Delta x} = \sum_{q=-\infty}^{\infty} \delta(q - k_0 \Delta x / 2\pi) = \frac{2\pi}{\Delta x} \sum_{q=-\infty}^{\infty} \delta(k_0 - q \frac{2\pi}{\Delta x})$, we have,

$$\sum_{\mathbf{r}_f} e^{i(\mathbf{k}' - \mathbf{k}) \cdot \mathbf{r}_f} = 8\pi^3 \sum_{\mathbf{q}} \delta(\mathbf{k}' - \mathbf{k}_q). \quad (\text{B.1})$$

We have also used $\Delta x \Delta y \Delta z = 1$. The infinite sum in Eq. (2.3) is related to the infinite sum on the reference grid, Eq. (B.1), by a phase factor,

$$\sum_{\mathbf{r}_\rho} e^{i(\mathbf{k}' - \mathbf{k}) \cdot \mathbf{r}_\rho} = e^{i(\mathbf{k}' - \mathbf{k}) \cdot \Delta \mathbf{r}_\rho} \cdot \sum_{\mathbf{r}_f} e^{i(\mathbf{k}' - \mathbf{k}) \cdot \mathbf{r}_f} = 8\pi^3 \sum_{\mathbf{q}} \psi(\mathbf{q} \cdot \mathbf{k}_g, \Delta \mathbf{r}_\rho) \delta(\mathbf{k}' - \mathbf{k}_q) \quad (\text{B.2})$$

where $\mathbf{r}_\rho = \mathbf{r}_f + \Delta \mathbf{r}_\rho$ and $\psi(\mathbf{q} \cdot \mathbf{k}_g, \Delta \mathbf{r}_\rho) = e^{i(\mathbf{q} \cdot \mathbf{k}_g) \cdot \Delta \mathbf{r}_\rho}$ is the phase factor. For zero offset $\Delta \mathbf{r}_\rho = (0, 0, 0)$, $\psi = 1$; while for a half cell offset, ψ is either 1 or -1 , e.g. if $\Delta \mathbf{r}_\rho = (\Delta x/2, 0, 0)$, $\psi = (-1)^n$.

Appendix C. Linear dispersion of electrostatic PIC models

The linear numerical dispersion of the momentum conserving and energy conserving PIC models are given in [1] for finite time step. Here we gives a similar derivation but without introducing temporal aliasing, as all PIC quantities, including the distribution function, are discrete in time. The perturbed discrete (in time) distribution function is derived in a way similar to Eq. (30) of [8] but with one full position update instead of two half updates,

$$\tilde{f}_1(\mathbf{k}, \mathbf{v}, \omega) = \frac{-i\Delta t e^{-i(\omega - \mathbf{k} \cdot \mathbf{v})\Delta t/2}}{2} \csc[(\omega - \mathbf{k} \cdot \mathbf{v})\Delta t/2] \tilde{\mathbf{F}}(\mathbf{k}, \omega) \cdot \nabla_{\mathbf{v}} f_0, \quad (\text{C.1})$$

for which a phase factor $e^{i\omega\Delta t/2}$ is dropped because f_1 is now needed at the same time step as the electric field.

When the leap-frog update is viewed as a continuous time integration of the Newton's laws but with a force sampled on the time step, temporal aliasing is introduced. In such case the distribution function of the eigen mode is defined on the continuous time, and the discrete distribution function in PIC is its time sample. The linearization is performed on the former and before the time sampling. Using $\sum_q \frac{1}{\omega - \mathbf{k} \cdot \mathbf{v} - 2\pi q/\Delta t} = \frac{\Delta t}{2} \cot[(\omega - \mathbf{k} \cdot \mathbf{v})\Delta t/2]$ to evaluate the infinite sum from aliasing [1], one arrives at a similar expression to Eq. (C.1) for the perturbed discrete distribution function but with $e^{-i(\omega - \mathbf{k} \cdot \mathbf{v})\Delta t/2} \csc[(\omega - \mathbf{k} \cdot \mathbf{v})\Delta t/2] = \cot[(\omega - \mathbf{k} \cdot \mathbf{v})\Delta t/2] - i$ replaced by $\cot[(\omega - \mathbf{k} \cdot \mathbf{v})\Delta t/2]$. This difference does not manifest in the zeroth moment of \tilde{f}_1 but may appear in higher order moments.

The normalized equations for the perturbed density $\tilde{\rho}_1(\mathbf{k}, \omega)$, the potential $\tilde{\phi}_1(\mathbf{k}, \omega)$, the electric field $\tilde{\mathbf{E}}_1(\mathbf{k}, \omega)$ and the force $\tilde{\mathbf{F}}(\mathbf{k}, \mathbf{v}, \omega)$ are,

$$\tilde{\rho}_1(\mathbf{k}, \omega) = \sum_{\mathbf{q}} \tilde{S}_\rho(\mathbf{k}_q) \int \tilde{f}_1(\mathbf{k}_q, \mathbf{v}, \omega) d\mathbf{v}, \quad (\text{C.2})$$

$$\tilde{\phi}_1(\mathbf{k}, \omega) = \tilde{\rho}_1(\mathbf{k}, \omega)/[\mathbf{k}]^2, \quad (\text{C.3})$$

$$\tilde{\mathbf{E}}_1(\mathbf{k}, \omega) = -i\boldsymbol{\kappa}(\mathbf{k})\tilde{\phi}_1(\mathbf{k}, \omega), \quad (\text{C.4})$$

$$\tilde{\mathbf{F}}(\mathbf{k}, \omega) = \tilde{S}_E(\mathbf{k})\tilde{\mathbf{E}}_1(\mathbf{k}, \omega), \quad (\text{C.5})$$

where $[\mathbf{k}]^2$ is the Poisson operator and $\boldsymbol{\kappa}(\mathbf{k})$ is the gradient operator. All grid quantities are transformed according to the transform defined in Eq. (2.1). Eq. (C.2) also implies that $\Delta \mathbf{r}_\rho = 0$ is chosen in Eq. (2.8), so $\psi(\mathbf{q} \cdot \mathbf{k}_g, \Delta \mathbf{r}_\rho) = 1$.

Substituting Eq. (C.1) into the above equations, the dispersion equation is,

$$1 + \frac{1}{[k]^2} \sum_{\mathbf{q}} \tilde{S}_\rho(\mathbf{k}_q) \tilde{S}_E(\mathbf{k}_q) \int \frac{\Delta t e^{-i(\omega - \mathbf{k}_q \cdot \mathbf{v})\Delta t/2}}{2} \csc[(\omega - \mathbf{k}_q \cdot \mathbf{v})\Delta t/2] [\kappa] \cdot \nabla_{\mathbf{v}} f_0 d\mathbf{v} = 0. \quad (\text{C.6})$$

For a cold uniform beam with velocity \mathbf{v}_0 , it reduces to,

$$1 - \left(\frac{\Delta t}{2} \right)^2 \frac{1}{[k]^2} \sum_{\mathbf{q}} \frac{\tilde{S}_\rho(\mathbf{k}_q) \tilde{S}_E(\mathbf{k}_q) \kappa(\mathbf{k}_q) \cdot \mathbf{k}_q}{\sin^2[(\omega - \mathbf{k}_q \cdot \mathbf{v}_0)\Delta t/2]} = 0. \quad (\text{C.7})$$

Eq. (C.7) has many resonances that are folded into the fundamental Brillouin zone $-\pi < \omega\Delta t/2 \leq \pi$. For two interacting resonances, the dispersion equation can be simplified as $1 - a[\sin^{-2}(y) + b\sin^{-2}(y+c)] = 0$, $|b| < 1$. Here we use the 1D case and include the fundamental mode and the q th ($|q| > 0$) alias mode as an example, $y = (\omega - k \cdot \mathbf{v}_0)\Delta t/2$, $a = \Delta t^2 \tilde{s}_\rho(k) \tilde{s}_E(k) \kappa(k) k / 4[k]^2 \geq 0$, $b = \tilde{s}_\rho(k_q) \tilde{s}_E(k_q) \kappa(k_q) k_q / \tilde{s}_\rho(k) \tilde{s}_E(k) \kappa(k) k$, and $c = (qk_g v_0 \Delta t / 2) \bmod 2\pi$, $-\pi < c \leq \pi$. When Δt is sufficiently small, this equation can be approximated by a quartic equation in y , $-acy^2 + (-a - ab + c^2)y^2 - 2cy^3 + y^4 = 0$, for which a pair of complex conjugate roots (the other two roots are always real) exist when the discriminant $D = -16a^2bc^2 [(a(1+b) - c^2)^3 - 27a^2bc^2] < 0$. When $D > 0$, there are (1) four real roots, if $a > 0$; or (2) two pairs of complex conjugate roots, if $a < 0$. Therefore, for the interaction of any two nearby resonances, there are domains of stability/instability defined by the parameters a, b and c , depending on the signs of D and a .

Two types of situation can be distinguished. When $b > 0$, the simplified dispersion equation resembles that of a physical two-stream instability. Stability requires $(a(1+b) - c^2)^3 - 27a^2bc^2 \leq 0$ and $a > 0$, which gives a stable domain $0 < a < a_1$ and unstable domains $a > a_1$ or $a < 0$. Here a_1 is the only real root of $(a(1+b) - c^2)^3 - 27a^2bc^2 = 0$. For $|b| \ll 1$, $a_1 \approx (1 - 3b^{1/3})c^2$. When $b < 0$, which corresponds to unusual two streams with densities of opposite signs, the stable domain is $a > a_1$ and the unstable domain is $a < a_1$.

The dispersion equation Eq. (C.7) applies to both the energy conserving and momentum conserving PIC models. The major difference in Eq. (C.7) for these two PIC models is the operator $\kappa(k_q)$. For the energy conserving model, $\kappa(k_q) = k_q$, so $b \sim k_q^2 > 0$. Therefore, interaction of any pair of resonances is of the usual two-stream type and there is a stable domain $0 < a < a_1$. This can be written explicitly, e.g., for the fundamental mode and the q th ($|q| > 0$) alias mode, $[(qk_g v_0 \Delta t / 2) \bmod 2\pi]^2 > \frac{\Delta t^2}{4[k]^2} \tilde{s}_\rho(k) \tilde{s}_E(k) \kappa(k) k [1 - 3(\tilde{s}_\rho(k_q) \tilde{s}_E(k_q) \kappa(k_q) k_q / \tilde{s}_\rho(k) \tilde{s}_E(k) k^2)^{1/3}]^{-1}$. For momentum conserving PIC model, $\kappa(k_q) = k_q \text{sinc}(k_q \Delta x)$, so $b \sim k_q^2 \text{sinc}(k_q \Delta x)$ which switches sign when q switches sign. Therefore, interaction of any pair of resonances can be of either the first or the second type.

References

References

- [1] C. K. Birdsall, B. A. Langdon, Plasma Physics via Computer Simulation, IOP Publishing Ltd., Bristol, England, 1991.
- [2] B. A. Langdon, Effects of the spatial grid in simulation plasmas, Journal of Computational Physics 6 (2) (1970) 247–267.

- [3] H. Okuda, Nonphysical noises and instabilities in plasma simulation due to a spatial grid, *Journal of Computational Physics* 10 (3) (1972) 475–486.
- [4] B. B. Godfrey, Numerical Cherenkov instabilities in electromagnetic particle codes, *Journal of Computational Physics* 15 (4) (1974) 504–521.
- [5] B. B. Godfrey, J.-L. Vay, Numerical stability of relativistic beam multidimensional PIC simulations employing the Esirkepov algorithm, *Journal of Computational Physics* 248 (2013) 33–46.
- [6] X. Xu, P. Yu, S. F. Martins, F. S. Tsung, V. K. Decyk, J. Vieira, R. A. Fonseca, W. Lu, L. O. Silva, W. B. Mori, Numerical instability due to relativistic plasma drift in em-pic simulations, *Computer Physics Communications* 184 (11) (2013) 2503 – 2514.
- [7] E. Lindman, Dispersion Relation for Computer-Simulated Plasmas, *Journal of Computational Physics* 5 (1) (1970) 13–22.
- [8] M. D. Meyers, C.-K. Huang, Y. Zeng, S. Yi, B. J. Albright, On the numerical dispersion of electromagnetic particle-in-cell code: Finite grid instability, *Journal of Computational Physics* 297 (2015) 565–583.
- [9] C. K. Birdsall, N. Maron, Plasma self-heating and saturation due to numerical instabilities, *Journal of Computational Physics* 36 (1) (1980) 1–19.
- [10] L. Chen, B. A. Langdon, C. K. Birdsall, Reduction of the Grid Effects in Simulation, *Journal of Computational Physics* 14 (1974) 200–222.
- [11] J. Brackbill, G. Lapenta, A Method to Suppress the Finite-Grid Instability in Plasma Simulations, *Journal of Computational Physics* 114 (1) (1994) 77–84.
- [12] H. R. Lewis, A. Sykes, J. A. Wesson, A comparison of some particle-in-cell plasma simulation methods, *Journal of Computational Physics* 10 (1) (1972) 85–106.
- [13] H. R. Lewis, Energy-conserving numerical approximations for Vlasov plasmas, *Journal of Computational Physics* 6 (1) (1970) 136–141.
- [14] G. Chen, L. Chacón, D. C. Barnes, An energy- and charge-conserving, implicit, electrostatic particle-in-cell algorithm, *Journal of Computational Physics* 230 (18) (2011) 7018–7036.
- [15] S. Markidis, G. Lapenta, The energy conserving particle-in-cell method, *Journal of Computational Physics* 230 (18) (2011) 7037–7052.
- [16] W. T. Taitano, D. A. Knoll, L. Chacón, G. Chen, Development of a Consistent and Stable Fully Implicit Moment Method for Vlasov–Ampère Particle in Cell (PIC) System, *SIAM Journal on Scientific Computing* 35 (5) (2013) S126–S149.
- [17] J. Xiao, J. Liu, H. Qin, Z. Yu, A variational multi-symplectic particle-in-cell algorithm with smoothing functions for the Vlasov-Maxwell system, *Physics of Plasmas* 20 (10) (2013) 102517.
- [18] J. Xiao, H. Qin, J. Liu, Y. He, R. Zhang, Y. Sun, Explicit high-order non-canonical symplectic particle-in-cell algorithms for Vlasov-Maxwell systems, *Physics of Plasmas* 22 (11) (2015) 112504.
- [19] G. Vlad, S. Briguglio, G. Fogaccia, B. Martino, Gridless finite-size-particle plasma simulation, *Computer Physics Communications* 134 (1) (2001) 58–77.
- [20] V. K. Decyk, Description of Spectral Particle-in-Cell Codes from the UPIC Framework, <http://picksc.idre.ucla.edu/publications/publications-reports-and-notes/>, accessed: 2015-07-30.
- [21] E. G. Evstatiев, B. A. Shadwick, Variational formulation of particle algorithms for kinetic plasma simulations, *Journal of Computational Physics* 245 (2013) 376–398.
- [22] G. Lapenta, J. U. Brackbill, P. Ricci, Kinetic approach to microscopic-macroscopic coupling in space and laboratory plasmas, *Physics of Plasmas* 13 (5) (2006) 055904.